Remote Sensing of Environment 315 (2024) 114480

Contents lists available at ScienceDirect

Remote Sensing of Environment

journal homepage: www.elsevier.com/locate/rse

4D imaging of the volcano feeding system beneath the urban area of the Campi Flegrei caldera

Pietro Tizzani [a,b,1], José Fernández [c,1,*], Andrea Vitale [d,b], Joaquín Escayo [c,2], Andrea Barone [a,b], Raffaele Castaldo [a,b], Susi Pepe [a,b], Vincenzo De Novellis [a,b], Giuseppe Solaro [a,b], Antonio Pepe [a], Anna Tramelli [e], Zhongbo Hu [c], Sergey V. Samsonov [f], Isabel Vigo [g], Kristy F. Tiampo [h], Antonio G. Camacho [c,1]

[a] National Research Council of Italy (CNR), Institute for the Electromagnetic Sensing of the Environment (IREA), 328 Diocleziano, 80124 Napoli, Italy
[b] GAIA iLAB at the CNR, ISAFOM Headquarters, Piazzale E. Fermi 1, 80055 Portici, Naples, Italy
[c] Institute of Geosciences (CSIC-UCM), C/ Doctor Severo Ochoa, 7, Ciudad Universitaria, 28040 Madrid, Spain
[d] National Research Council of Italy (CNR), ISAFOM, Portici, Italy
[e] Istituto Nazionale di Geofisica e Vulcanologia, Sezione di Napoli, Osservatorio Vesuviano sezione di Napoli dell'INGV, via Diocleziano, 328, 80124 Napoli, Italy
[f] Canada Centre for Mapping and Earth Observation, Natural Resources Canada, 580 Booth Street, Ottawa, ON K1A 0E4, Canada
[g] Dept. of Applied Mathematics, EPS, University of Alicante, E03080 Alicante, Spain
[h] CIRES and Geological Sciences, 216 UCB, University of Colorado, Boulder, CO 80309, USA

ARTICLE INFO

Editor Name: Jing M. Chen

Keywords:
Multiplatform satellite radar observation
Multiband radar observation
Inverse techniques
4D interpretation
Volcano feeding system
Campi Flegrei caldera

ABSTRACT

This paper describes an approach to analyze ground deformation data collected by InSAR (Interferometric Synthetic Aperture Radar) imaging the volcano feeding system (VFS) beneath a caldera. The approach is applied to the Campi Flegrei caldera in southern Italy, a densely populated area at high risk for volcanic eruption. The method is a 4D tomographic inversion that considers a combination of 3D pressure sources and dislocations (strike-slip, dip-slip and tensile) acting simultaneously. This is in contrast to traditional methods that assume a priori geometries and type for the volcanic source. Another novelty is that we carry out a time-series analysis of multifrequency InSAR displacement data. The analysis of these multiplatform and multifrequency InSAR data from 2011 to 2022 reveals an inflating source at a depth of 3–4 km that is interpreted as a pressurized magmatic intrusion. The source broadens and migrates laterally over time, with a possible new magmatic pulse arriving in 2018–2020. The model also identifies a shallow region (at 400 m depth) that may be feeding fumaroles in the area. The analysis also reveals a zone of weakness (dip-slip) that could influence the path of rising magma. This method provides a more detailed dynamic 4 - dimensional image of the VFS than previously possible and could be used to improve hazard assessments in active volcanic areas.

1. Introduction

More than 800 million people live within 100 km of a volcano with the potential to erupt (Loughlin et al., 2015), which means a significant risk of destruction for property and infrastructure and loss of lives. Detecting the ascent of magma from depth and its accumulation in a shallow and/or intermediate reservoir can provide a warning for future eruptive activity (Sparks et al., 2012; Fernández et al., 2017); one of the major implications of the ascent of magma is the deformation at surface, which can be detected by several methodologies, such as the geodetic measurements. In recent decades there has been a notable increase in the number and quality of volcano geodetic data that significantly extended the spatial and temporal resolution and coverage (see e.g., Anderssohn et al., 2009; Arab-Sedze et al., 2014; Jo et al., 2015; Kubanek et al., 2015; Chen et al., 2017; Deng et al., 2019; Pepe et al., 2019; Di Traglia et al., 2021; Saroli et al., 2021; Poland and Zebker, 2022; Fernández et al., 2022; Amoruso and Crescentini, 2023; Naranjo et al., 2023; and references therein).

* Corresponding authors.
E-mail address: jft@mat.ucm.es (J. Fernández).
[1] These authors contributed equally: Pietro Tizzani, José Fernández, Antonio G. Camacho.
[2] Current address: ETS de Ingenieros en Topografía, Geodesia y Cartografía, Universidad Politécnica de Madrid, 28031-Madrid, Spain

https://doi.org/10.1016/j.rse.2024.114480
Received 22 December 2023; Received in revised form 14 October 2024; Accepted 17 October 2024
Available online 22 October 2024

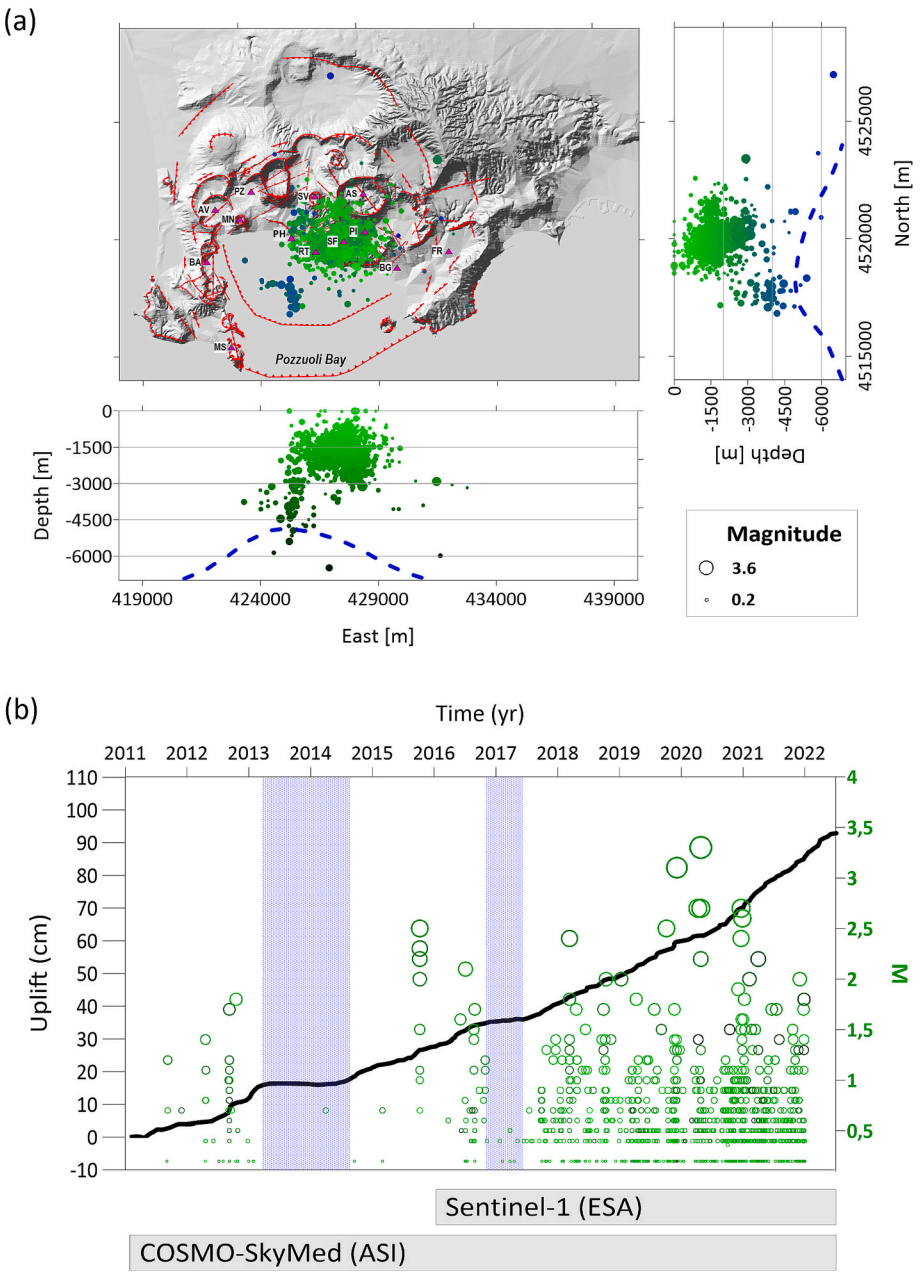

Fig. 1. Seismic and geodetic data. (a) Shaded relief map of CFc SRTM-DEM (https://dwtkns.com/srtm30m/ UTM-WGS84 projection zone is 33 N) and 2011–2022 seismicity (green circles); the circles are scaled in size with different magnitudes along EW and NS vertical sections. The dashed blue line represents the Brittle/Ductile transition (from Castaldo et al., 2019); magenta lines show the outcropping faults, the Campanian Ignimbrite (CI) and Neapolitan Yellow Tuff (NYT) caldera borders and outer/inner rims (after: De Siena et al., 2017; Natale et al., 2022; Natale et al., 2024; modified). The magenta triangles represent the sites referred in the text: Pozzuoli (PZ), Fuorigrotta (FR), Averno (AV), Capo Miseno (MS), Astroni crater (AS), Solfatara crater (SF), Pisciarelli fumarole spring (PI), Bacoli (BA) and San Vito (SV). (b) Vertical displacement time series (black line) recorded by cGPS RITE (RIone TErra, RT) station in the 2011–2022 time interval. The green circles indicate the seismicity with different sizes (magnitude). The shadowed blue region marks very-low seismic frequency intervals. The grey bars specify the time intervals of multiplatform SAR acquisitions shown in Fig. 2.

Multi-platform radar remote sensing of volcanic areas is a valuable tool to detect ground deformation at volcanos and to infer the geometry of a Volcano Feeding System (VFS), which is essential information for detecting and characterizing unrest and eruption episodes. The availability of long-term (spanning decades) deformation data from satellite observations, with an extensive spatial coverage and high spatial resolution, opens new possibilities for volcano monitoring (Sparks et al., 2012; Fernández et al., 2017; Widiwijayanti et al., 2024). These new and large datasets cannot be wholly exploited using the classical approach for interpretation (Bonaccorso et al., 2005; Lisowski, 2007; Camacho and Fernández, 2019; Crozier et al., 2023), and there is a real need for new approaches for analyzing, modelling and interpreting (Fernández et al., 2017; De Matteo et al., 2022; Barone et al., 2022a, 2022b). The classical approaches usually assume a priori geometries and nature of the source, inverting separately for the different sources when more than one is considered. Additionally, complicated ground deformation patterns are present in many volcanic active areas due to the simultaneous impact of multiple natural magmatic/hydrothermal and anthropogenic sources (Troise et al., 2019; Camacho et al., 2020 and references therein). For this reason, it is necessary to consider distributed sources acting simultaneously for an interpretation of the observed surface deformation during the inversion of the geodetic data.

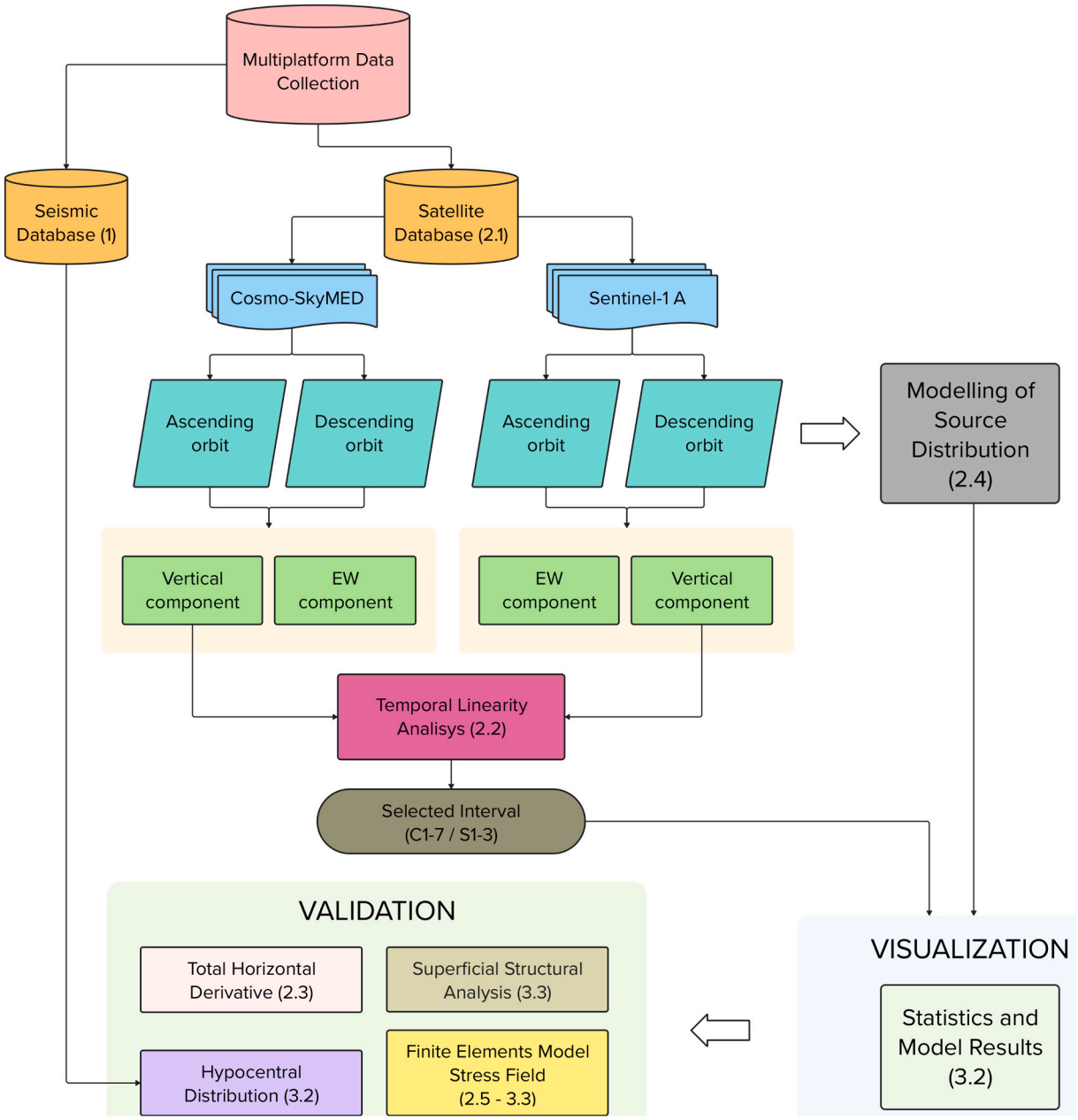

Flowchart 1. Employed method. The number in brackets indicates the manuscript sections.

In this paper, we applied this methodology to one of the most deforming and densely populated volcanic area in the world, the Campi Flegrei caldera (CFc), in Southern Italy (Chiodini et al., 2012; Castaldo et al., 2019; Siniscalchi et al., 2019; Petrillo et al., 2023). A resumption of its eruptive activity might involve the potential evacuation of more than 500,000 people and damage to more than 2400 buildings, up to 200 km of roads, and 17 km of the high-voltage electricity network (Charlton et al., 2020) in the CFc area. Therefore, the study of the VFS and its spatial-temporal evolution is a key point to improve the understanding of a future eruptive scenario. In particular, we apply the geodetic tomographic inversion approach already used to other volcanoes [Mt. Etna, Italy, and Cumbre Vieja, La Palma, Canary Islands, Spain (Camacho et al., 2020; Fernández et al., 2021, 2022, 2024)] to carry out a 4D imaging of VFS geometry and its time evolution. This inversion method, unlike to traditional approaches, considers a combination of 3-D arbitrary sources for pressure and dislocations (strike-slip, dip-slip and tensile), which can act simultaneously and are adjusted without any a-priori hypotheses on the nature, shape or positioning of the source (Fernández et al., 2022, 2024). A time-series analysis is done allowing to study the time evolution of the sources.

Past and recent studies employing different inversion techniques (see e.g., Dzurisin, 2007; Fernández et al., 2009; Sigmundsson et al., 2010; Camacho et al., 2011; Samsonov et al., 2014; Cannavò et al., 2015; Tizzani et al., 2015; Camacho et al., 2020; Fernández et al., 2017; Fernández et al., 2021; and references therein), allowed detecting the shallow region of the VFS (0–5 km) and part of the mid-crustal portion (5–10 km) at specific time intervals (see e.g., Fernández et al., 2001; Dzurisin, 2007; Trasatti et al., 2008; González et al., 2013; Camacho and Fernández, 2019; and references therein), although the spatial-temporal coverage of the deformation data and the inversion limitations interfere with resolution in depth.

1.1. Campi Flegrei caldera: Background and recent activity

CFc is a volcanic field at least 80 ka old, characterized by a nested collapsed caldera structure (Luongo et al., 1991; Cubellis et al., 1995; Vitale and Isaia, 2014), and dotted by several volcanic edifices and structural alignments (e.g., Di Vito et al., 2016) (Fig. 1a). The caldera structure is the result of at least two large eruptions, namely the Campanian Ignimbrite (Gallo et al., 2024) at 39 ka and the Neapolitan Yellow Tuff (Orsi et al., 1992) dated at 14.5 ka.

The long-term caldera deformation, observed since 10 ka (Isaia et al., 2009; Natale et al., 2022), has been characterized by alternating slow subsidence phenomena and rapid resurgence phases of the caldera floor and preceded Mt. Nuovo eruption (1538 CE; Di Vito et al., 2016). Since 1905, the ground-based topographic levelling networks, recently integrated with a Global Navigation Satellite System (GNSS) monitoring network and satellite data, have been recording the unrest episodes affecting the inner caldera area (Del Gaudio et al., 2010). Major uplifts of 170 and 180 cm were estimated at Pozzuoli harbor in 1970–71 and 1982–85, respectively (De Natale et al., 2006; Del Gaudio et al., 2010). This latter unrest episode was followed by three distinctive displacement phases: (i) prevailing long-term subsidence (1985–2000) detected via high precision spirit-levelling measurements (Dvorak and Berrino, 1991; Del Gaudio et al., 2010) and satellite data (Lanari et al., 2004), (ii) low deformation rates (2000−2012), detected via GNSS measurements and geochemical data (Petrillo et al., 2023) interrupted by a series of high-frequency mini-uplift episodes (2000; 2005; 2012) and finally (iii) a new uprising background upheaval, detected via GNSS measurements and satellite data (Pepe et al., 2019; Castaldo et al., 2021; Polcari et al., 2022). From 2011 to 2018, GNSS data at RITE station revealed a considerable uplift with an average deformation rate of about 9 cm/year, except for the 2013.2–2014.6 and 2016.8–2017.4 periods (green shadow interval in Fig. 1b), when a substantial deceleration was detected (Charlton et al., 2020; Pepe et al., 2019; Castaldo et al., 2021; Bevilacqua et al., 2022; Polcari et al., 2022; Falanga et al., 2023; Petrillo et al., 2023). Subsequently, in the 2017.5–2022.5 time interval (Fig. 1b), an acceleration of uplift with an average deformation rate of about 11 cm/year occurred (e.g., Bevilacqua et al., 2022; Vitale and Natale, 2023).

Regarding the thermo-rheological conditions of the crust beneath the caldera, Castaldo et al. (2019) demonstrated the presence of a primary thermal source located beneath Pozzuoli Bay, reaching a temperature of about 800 °C at a depth of 6 km. The same isotherm is situated outside the caldera region at a depth of about 20 km, revealing a higher horizontal gradient of temperature (see figs. 5 and 9 of Castaldo et al., 2019). This thermal distribution produced a Brittle/Ductile (B/D) transition at a shallower depth beneath the caldera floor. More than 90 % of the recorded seismic events are located above the B/D transition. Zollo et al. (2008), starting from the modelling of magma properties, based on measured seismic velocities, identified a melting zone with a relatively high melt percentage in the 65–90 % range, whereas shallower and smaller melt-rich portions were likely hindered by the resolution of the employed methodology. The horizontal extension of this melt layer spans at least 30 km^2, with an approximate thickness of 1 km, located at about 8 km depth; above this depth, several authors have proposed an oblate-like spheroid source ENE–WSW slightly oriented (Woo and Kilburn, 2010; D'Auria et al., 2015; Di Vito et al., 2016; Castaldo et al., 2021; Bonafede et al., 2022; Amoruso and Crescentini, 2023). These results are also consistent with the observed distribution of earthquake hypocenters (Fig. 1a). Along the coast, the innermost region of the caldera is affected by clustering of seismicity, with more than 90 % of earthquakes localized between 1 and 4 km depth, most of them localized in the Solfatara-Pisciarelli area (e.g. Isaia et al., 2021; Scotto di Uccio et al., 2024). Accordingly, the spatial distribution of the strain and energy release reaches a maximum of about 2 km and becomes negligible below 3 km depth (Castaldo et al., 2019). Intense seismic activity is also observed during these deformation unrests. Fig. 1a shows the relocated seismicity recorded in CFc by the INGV-Osservatorio Vesuviano network since 2011; this catalogue includes more than 2000 volcano-tectonic earthquakes with a magnitude greater or equal to zero (Tramelli et al., 2022). Their spatial distribution shows depths above 8 km and a low magnitude cluster below Solfatara/Pisciarelli (SF/PI) areas at shallow depths usually above 3 km b.s.l.. Another seismogenic area is highlighted offshore with an NW-SE epicentral distribution, where the recorded earthquakes have hypocentral depths between 2 and 4 km b.s.l.. These areas were identified during the 1982–84 bradyseismic crisis (D'Auria et al., 2011). An increase in the number and magnitude of the recorded earthquakes occurred from 2011 to 2022 (Fig. 1a). These earthquakes have been relocated and delineate the inner caldera fault as shown in Scotto di Uccio et al. (2024). Two intervals with an abrupt decrease in seismic activity have also been observed (between 2013 and 2014 and around 2017), and this occurred in correspondence with a reduction of the deformation rate as well (Fig. 1b) (Bevilacqua et al., 2022).

2. Methods

The integrated methodology employed in this paper is summarized in Flowchart 1 and described below. Starting from the multiplatform data, we processed satellite data from Cosmo-Sky-Med (CSK) and Sentinel-1 (S-1) platforms acquired along ascending and descending orbits. Both sets of data were used as input for the geodetic tomographic inversion process, providing us a spatial-temporal distribution of pressure and dislocation sources within the crust.

To fully exploit the spatial-temporal evolution of the ground deformation pattern, we show both vertical and EW components. In particular, the vertical component is used to identify the linear deformation intervals through the Temporal Linearity Analysis method, while the EW component allows us to emphasize the asymmetry of ground deformation field. The estimated time windows represent the start and end points of the identified linear deformation events. Finally, to validate the modelled solutions we compare the achieved results against other relevant information, including the distribution of seismic hypocenters, the density distribution of surface structures, and results from additional data analysis techniques such as Total Horizontal Derivative (THD) and Finite Element (FE) stress field model.

2.1. DInSAR processing

The ground deformations of CFc have been retrieved by applying the Differential Interferometric Synthetic Aperture Radar (DInSAR) methodology (Jolivet et al., 2011; Rosen et al., 2000; Massonnet et al., 1993; Gabriel et al., 1989) that allows generating spatially dense ground deformation maps with a centimeter-to-millimeter accuracy. DInSAR methods rely on the computation of the phase difference (i.e., an interferogram) between two temporally separated SAR images, accounting for the measured projection of the surface deformation along the radar-to-target Line of Sight (LOS) direction. The results presented in this study have been carried out by applying the multi-temporal Small BAseline Subset (SBAS) approach (Berardino et al., 2002), which allows detection and characterization of the temporal evolution of ground deformation phenomena via the generation of LOS-projected ground displacement time series and relevant displacement velocity maps over the entire period of observation, referred to a stable pixel. To achieve this task, SBAS implements a pixel-by-pixel straightforward combination of a selected set of multi-looked, unwrapped DInSAR interferograms related to SAR data pairs characterized by short spatial and temporal separations (short baselines), thus mitigating the effects of decorrelation noise signals in the generated ground deformation products. In general, such a preliminary SAR data pair selection might determine the entire SAR dataset and can be fragmented into independent sets of images separated by large baselines, which are then straight forwardly linked by applying the Singular Value Decomposition (SVD) method. This

primarily affects Cosmo-SkyMED (CSK) data, since Sentinel-1 (S-1) is engineered for having a small baseline.

Our study exploits the archives of C-band and X-band SAR ($\lambda = 5.56$ cm and $\lambda = 3.1$ cm respectively) data collected from 2011 to 2022 over the study area from ascending and descending orbits acquired from the CSK and the S-1 satellite constellations. The different operational carrier frequencies of CSK and S-1 satellite data lead to specific benefits and limitations. Indeed, the precision of DInSAR ground deformation measurements rigorously depends on the wavelengths employed and is improved at lower wavelengths (i.e., at X band); conversely, the DInSAR phases extracted from images gathered at higher wavelengths (i.e., at C band) are less affected by decorrelation noise artifacts. Therefore, the joint exploitation of multi-frequency data allows for the maximum reduction in pixel loss and reduction in error. Furthermore, the combined use of multi-platform SAR data collected at different epochs enhances the temporal sampling of the attainable displacement products (i.e., time series).

Specifically, for the CSK catalogue, starting from the available data, we considered ascending and descending orbit acquisitions over the area by using 338 and 127 images, respectively, between October 2011 and February 2022. Complimentarily, we used the S-1 SAR data available over CFc from October 2014 to 2022 collected through the Interferometric Wide (IW) mode. In this study, we considered both the ascending and descending orbits. The single-look-complex (SLC) SAR images were downloaded from Alaska Satellite Facility DAAC (https://asf.alaska.edu/), resulting in 186 acquisitions for the ascending orbit and 179 for the descending one.

Both Sentinel 1A and Sentinel 1B SAR data were considered. Accordingly, the minimum temporal separation between SAR acquisitions was 6 days. For the used CSK SAR dataset, a minimum revisit time of 8 days was exploited.

For both SAR datasets, a sequence of short baseline interferometric SAR data pairs were selected, with a maximum allowed temporal baseline of 96 days and no constraints on the maximum perpendicular baseline applied. Then, the selected SAR interferograms were generated, unwrapped (Pepe and Lanari, 2006) and finally inverted using the SBAS technique (Berardino et al., 2002), considering a point located in the center of Napoli as the reference point for the DInSAR products (437175 m E, 4521791 m N). For the generation of differential SAR interferograms, precise orbital information (https://s1qc.asf.alaska.edu/aux_poeorb/) was used to process the SAR data; the phase contributions due to the topography were also reconstructed using the NASA Shuttle Radar Topography Mission (SRTM) Version 3.0 Global 1 arc *sec* (SRTMGL1) data (https://dwtkns.com/srtm30m/) of the study area.

The availability of ascending and descending SAR data sets allowed us to generate a time series of the vertical and east-west ground displacement components. We combined the geocoded displacement maps computed from the ascending and descending orbits on high-coherent points common to both orbits, considering the different multi-platform acquisition geometries of CSK and S-1. Highly coherent and well processed points were identified for every used SAR dataset by computing the temporal coherence factor (Pepe and Lanari, 2006) that jointly accounts for decorrelation noise and phase unwrapping mistakes. More specifically, a temporal coherence threshold of 0.7 was applied to identify the final group of high-coherent points.

2.2. Temporal linearity analysis method

To analyze the coherent information content in the processed signals, we developed a mathematical approach to detect the temporal linearity behaviors inside a non-linear deformation time series relevant to the CFc case study. For this purpose, we consider the vertical component of ground deformation in order to compare the independent CSK and S-1 datasets; we select the vertical deformation time series of the pixel with the max amplitude. The first step of Temporal Linearity Analysis (TLA) consists in applying a smoothing function to the time series. This step helps to remove the high-frequency oscillations that could be related to the external noise source as the atmospheric artifacts or site effects. We used a smoothing spline s with the smoothing parameter p. The smoothing spline minimize function is reported in (1):

$$p\sum_i (y_i - s(x_i))^2 + (1-p)\int \left(\frac{d^2 s}{dx^2}\right) dx \quad (1)$$

where p is defined between 0 and 1, $p = 0$ produces a least-squares straight-line fit to the data, while $p = 1$ produces a cubic spline interpolant. In our case, we used $p = 0.98$ to remove the high frequency oscillations signal component.

Once the high-frequency component is removed, it is possible to derivate the smoothed time series (s). We calculate the second-order derivative modulus ($|s''|$) of (s); its maxima identify the bounds of each time interval characterized by strongly linear behavior. The detected maximum amplitude of $|s''|$ will identify each linear interval, because they are related the deformation rate changes. This approach, compared to the classic moving average method is less affected by the high frequency oscillations related to noisy dataset.

To select the different linear intervals, we fix a threshold of 0.3 cm/yr on the deformation rate difference via trial and error: when a range has a value less than 0.3 cm/yr, it could be merged with the previous range, if it is higher, the range would represent a different deformation event. This threshold allows to recognize the deformation trend related to geodetic source from the local oscillation due to anthropogenic effects or other shallow signals.

We also performed a linear regression analysis for each interval estimated and the adjusted R^2 values are above 0.81 (0.93, 0.85, 0.99, 0.92, 0.99, 0.99, 0.99, for the C1–C7 intervals and 0.81, 0.99, 0.99, for the S1–S3 intervals), that are showing the goodness of the method to identify their linear behavior.

2.3. Total horizontal derivative method

The Total Horizontal Derivative (THD) technique detects the field source boundaries and horizontal position (Blakely, 1996). The method is based on analyzing the maxima of the horizontal gradient magnitude that is computed from the first order x- and y-derivatives of the considered field, recorded at the surface; in particular, the maxima distribution highlight at the surface where the discontinuities, in terms of the physical parameter of the detected field source (e.g. density for gravity field, pressure/volume for deformations), occur in depth, representing the horizontal boundaries of the sources. This is a powerful tool that provides reliable information, especially when the lateral contrasts of the investigated source physical parameter are abrupt and the size/depth ratio of the detected source increases.

The THD technique has been used to analyze sources producing different kinds of fields, such as potential fields (e.g., Florio et al., 1999; Cella and Fedi, 2015), P-wave velocity field (e.g., Gola et al., 2021) and deformation field (e.g., Pepe et al., 2019; Castaldo et al., 2021; Barone et al., 2022a, 2022b). In the case of deformations, we can define the THD_w as follows (Pepe et al., 2019):

$$THD_w = \sqrt{\left(\frac{\partial w(x,y,z)}{\partial x}\right)^2 + \left(\frac{\partial w(x,y,z)}{\partial y}\right)^2} \quad (2)$$

where w(x,y,z) represents the vertical component of the ground deformation at spatial coordinates (x,y,z) and horizontal derivatives are computed through finite-difference formulas. We specify that in volcanic frameworks the THD_w maxima may match, not only with the surface projection of magmatic reservoir boundaries, but also with deep structural heterogeneities. This occurs since the latter perturb the stress field at depth, which causes a deformation field at the surface affected by these structures, in turb behaving as secondary deformation sources (e.g., Pepe et al., 2019; Castaldo et al., 2021; Barone et al., 2022a, 2022b).

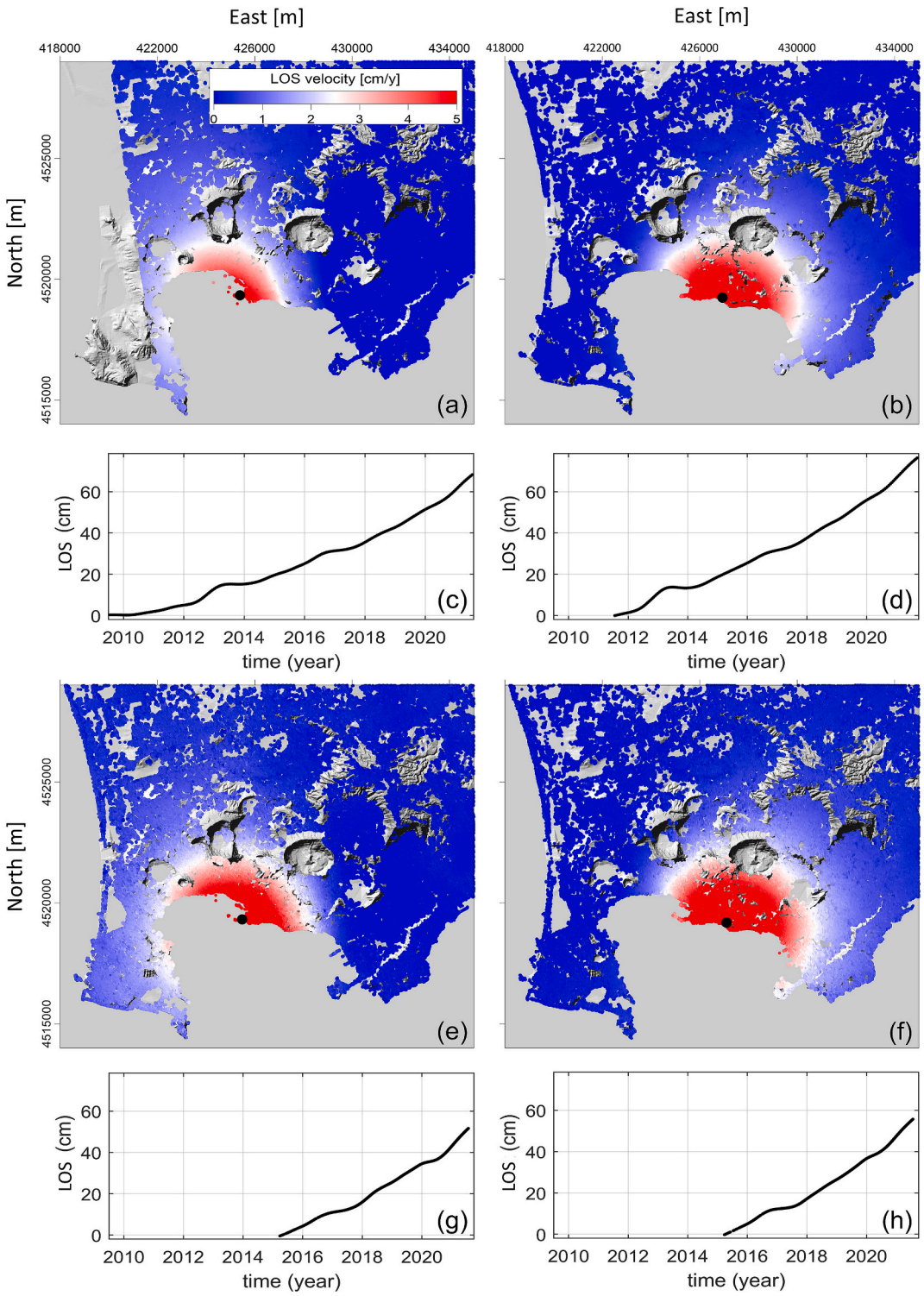

Fig. 2. DInSAR LOS displacement maps. (a, b) CSK LOS mean deformation velocity map along ascending and descending orbits, respectively and (c, d) the related LOS deformation time series relevant to the pixels with maximum displacement in the Pozzuoli harbor highlighted by the black dot in (a and b). (e, f) S-1 LOS mean deformation velocity map along ascending and descending orbits, respectively and (g, h) the related LOS deformation time series relevant to the pixels with maximum displacement in the Pozzuoli harbor highlighted by the black dot in (e and f).

2.4. Direct modelling and inverse technique

The interpretation methodology we use (Camacho et al., 2018; Camacho et al., 2020; Fernández et al., 2021, 2022, 2024) considers a combination of 3-D arbitrary sources for pressure and dislocations (strike-slip, dip-slip, and tensile) which can act simultaneously and are adjusted without any a priori hypotheses on the source nature, shape or location. The approach provides deformation sources as 3D cell aggregations for which the inversion process automatically assigns a source type, magnitude values (MPa for pressure and cm for dislocations), position and orientation (angles of dislocation planes). The inversion approach is nonlinear and is based on an exploratory approach to the

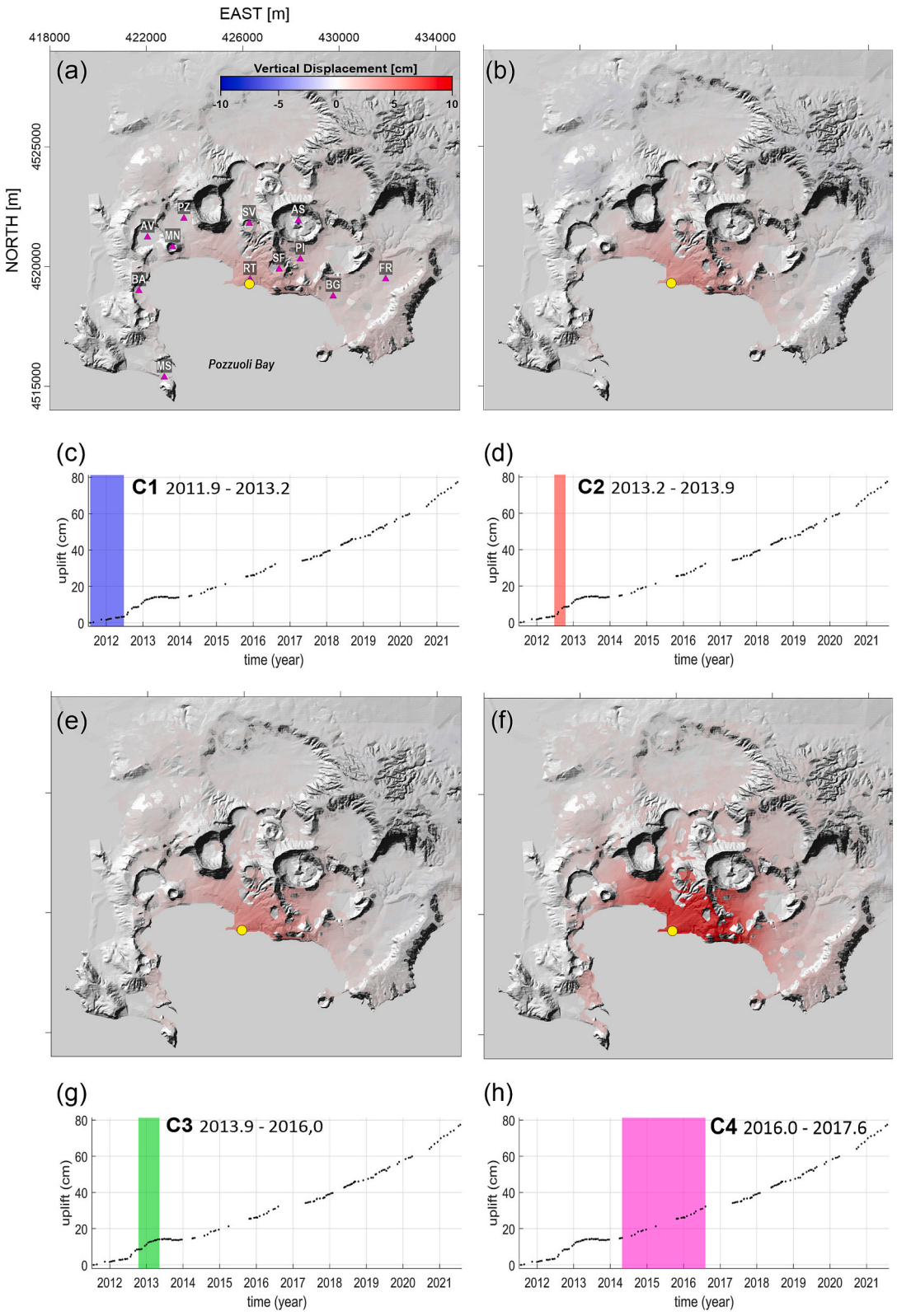

Fig. 3. DInSAR vertical displacement maps, superimposed on the shaded relief map of SRTM-DEM, for the first four time intervals (C1: 2011.6–2012.5, C2: 2012.5–2012.8, C3:2012.8–2013.3, C4:2014.3–2016.6), identified by the TLA algorithm. These maps were derived by combining CSK ascending and descending orbits. (a) vertical displacement map for the C1 time interval; (b) vertical displacement map for the C2 time interval; (e) vertical displacement map for the C3 time interval; (f) vertical displacement map for the C4 time interval. In (c, d, g, h), the vertical time series relative to the maximum vertical deformation pixel highlighted by a yellow dot and the identified linear time intervals with different colors are reported. (For interpretation of the references to colour in this figure legend, the reader is referred to the web version of this article.)

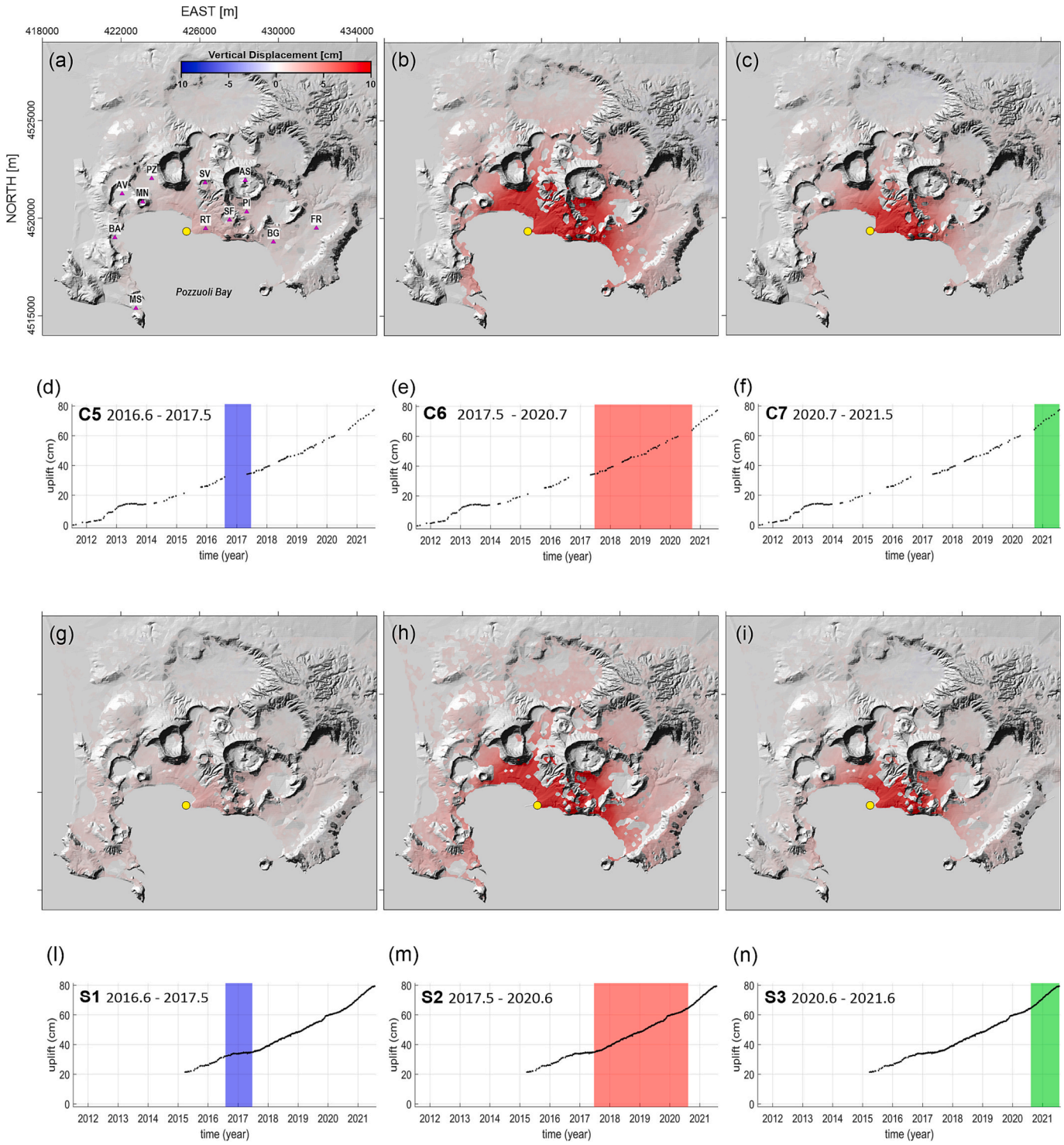

Fig. 4. DInSAR vertical displacement maps, superimposed on shaded relief map of SRTM-DEM, for the following three time intervals: C5: 2016.7–2017.6, C6: 2017.8–2020.5, C7:2020.6–2021.6 and S1: 2016.7–2017.6, S2: 2017.8–2020.5, S3:2020.6–2021.6, identified by the TLA algorithm. These maps were derived by combining CSK ascending and descending orbits for C5, C6 and C7 time intervals and S-1 ascending and descending orbits for S1, S2 and S3 time intervals. (a) vertical displacement map for the C5 time interval; (b) vertical displacement map for the C6 time interval; (c) vertical displacement map for the C7 time interval; (g) vertical displacement map for the S-1 time interval; (h) vertical displacement map for the S2 time interval; (i) vertical displacement map for the S3 time interval. In (d, e, f), the vertical time series relative to the maximum vertical deformation pixel highlighted by a yellow dot and the identified linear time intervals with different colors are reported in (l, m, n), as for (d, e, f) for the S-1 vertical time series component. (For interpretation of the references to colour in this figure legend, the reader is referred to the web version of this article.)

model space. This exploration is possible because of the use of a variable scale factor. The approach starts from a 3D grid of the entire subsurface volume divided into small prismatic cells and, using a step-by-step growth process successively fills selected cells with an adjusted type of deformation source and intensity values. The misfit functions are derived by the simultaneous fit of the data (LOS ascending and descending displacement data for all pixels) and a regularization condition based on the total size (strength) of the resulting anomalous model. A key balance factor allows a suitable trade-off between data fit and model regularity. Correct parameter selection is based on autocorrelation analysis of the final residuals. Planar, exact or homogeneously distributed data are not required. An intensity value (MPa·m^3) is assigned to each of the pressure sources obtained from the inversion process because the model equations do not allow separate pressure and volume values without assuming a particular value for one of the two parameters (see Methods section by Fernández et al. (2022)).

The methodology inverts simultaneously ascending and descending LOS displacement data from DInSAR, carrying out a time-series analysis. Successive deformation data sets corresponding to specific epochs T_i ($i = 1, \ldots, n$) can be modelled to recover the sources evolution, a non-standard feature in the classical approaches. Also, to consider a more regular modelling of the time-evolution of the sources, the inversion methodology (Fernández et al., 2022) moves from the irregular observation data epochs, T_i, to regular sampling times t_j ($j = 1, \ldots, m$) with a fixed sampling interval (e.g., 0.1 year). Additionally, in the inversion approach, for each epoch LOS deformation rates (cm/yr) are used as input deformation data values. For each pixel k, and epoch t_j, it obtains the value of deformation rate a_{jk}, d_{jk} (cm/yr) for ascending and descending LOS respectively. Finally, for each epoch t_j, the methodology gives the corresponding incremental 3D sources. This methodology incorporates the formulation of Geertsma and Van Opstal (1973) for pressure sources and Okada (1985) for dislocation sources. See the Methods section by Fernández et al. (2022) for more details.

Using only surface deformation data, it is difficult to distinguish between magmatic, hydrothermal, or volatile movement (Pritchard et al., 2019). However, this inversion methodology has shown in its application to the La Palma unrest and 2021 eruption (Fernández et al., 2021, 2022, 2024) its ability to help solve this limitation: the combination of pressure and dislocation sources provide a more accurate description of the subsurface. In case of a volatile source, there would be a pressure source only as inversion result, while in case of magmatic movement scenario displacement sources should be present as well. In the latter scenario, the magma viscosity generates a differential stress at surrounding rocks that produces these mechanisms at once. The methodology allows us to detect the ascent of magma indirectly by seeing the inversion results in the fractures produced and used by the magma in the ascent, as detected for La Palma.

2.5. 3D finite element stress model

In order to image the elastic stress field distribution in the crust, we constructed a Finite Element (FE) model by considering as input the retrieved distributed source from tomographic inversion. Specifically, we evaluated both the spatial distribution and direction of the stress tensor and magnitude of the von Mises stress (Castaldo et al., 2021) criterion as effect of the action of the over-pressure source beneath the Pozzuoli harbor (~1 km West to RT) for the C6 ≈ S3 time interval; this is the interval with the maximum cumulative vertical deformation. We first build up the 3D model geometry considering a domain of 22 × 16 × 10 km^3 and using the CFc topography. Specifically, the FE geometry is 10 km wider than these values in the x-y directions to reduce the effect of edges. Linear elastic isotropic mechanical properties were assumed, with a Young's modulus of 50 GPa, a Poisson's ratio of 0.25, and a density of 2400 kg/m^3. The first two elastic values represent the condition under of assumption linearity, isotropy and elasticity of the rocks. The selected density value is the average density of the rocks in the CFc area. The boundary conditions of the computational domain were chosen as fixed constraint at the bottom side and roller conditions at the lateral sides of the model. We discretized the computational domain using a mesh of tetrahedral elements whose dimension ranges from 250 to 1000 m, increasing size with depth.

Subsequently, we perform the forward model by applying a pressure increment value of 60 MPa on the external surface of the imported tomographic retrieved source.

3. Results

3.1. InSAR data analysis

We processed over 800 radar images acquired within the 2011–2022 time interval by two different SAR sensors namely Cosmo SkyMED and Sentinel-1(Fig. 2).

Several studies have widely analyzed the recent ongoing uplift of CFc (see e.g., Samsonov et al., 2014; D'Auria et al., 2015; Pepe et al., 2019; Castaldo et al., 2021; Polcari et al., 2022), modelling from the ground deformation signals the corresponding causative sources in the 2011–2015 time-interval. Pepe et al. (2019) have revealed that the spatial deformation pattern is asymmetric and characterized by different rates of deformation moving from the deformation center, close to Pozzuoli harbor, toward the borders of the CFc. In recent decades, the multi-platform, multifrequency, and multi-orbit SAR data have allowed us to collect coherent spatial and temporal high-resolution imaging of the ground deformation signals. Here, we benefit from the DInSAR data processing along the ascending and descending orbits, retrieving LOS mean deformation velocity maps and the corresponding deformation time series (Fig. 2). The ground deformation patterns provided us by the X-band (CSK) and C-band (S-1) satellite constellations are characterized by different geometric features, as a consequence of the different look angles and operating wavelengths of the employed sensors. To overcome this complexity and provide a homogeneous and unitary description of the ground deformation evolution for the considered time interval, we analyze the results regarding ground deformation components, such as the projection of the LOS along the vertical and the horizontal EW components. Specifically, we performed a detailed analysis of the CSK (Fig. 3; Fig. 4) and S-1 (Fig. 4) vertical ground deformation components by using the Temporal Linearity Analysis (TLA) (see Methods section) between 2011 and 2022.

The achieved results relevant to the vertical DInSAR displacements maps and corresponding time series for CSK results highlight the occurrence of clear uplift phases (C2, C4, C6, C7, S2, S3) alternating with periods of low deformation rate (C1, C3, C5, S1) (Fig. 3; Fig. 4) in agreement with GNSS data (INGV monthly bulletin).

Note that the vertical time series for CSK and S-1 are similar and characterized by linear and homogeneous trends, e.g., C5/S1, C6/S2, and C7/S3 (Fig. 4d, e, f, l, m, n). Both satellites are observing the same deformation, identifying the same process at each detected interval.

The C6/S2 interval differs from the other two (C5/S1 and C7/S3) for the uplift rates and the time length of the detected linearity interval. While in C6/S2, the linearity covers a time length of about three years, which can be considered a background behavior, the C5/S1 and C7/S3 linear intervals have a shorter time duration of about one year. In this latter case, the observed signals can be described as the effect of a powerful process. During the first interval, the caldera was affected by a generally broad low-intensity displacement field, with a maximum vertical displacement that reaches a value of about 3 cm around the Pozzuoli harbor (Fig. 4a, g). Subsequently, (interval C6/S2), the highest intensity value of vertical displacement of about 25 cm was found (Fig. 3b, h).

In contrast, in the area near the volcanic monogenic cones of Astroni (AS), *S. Vito* (SV) and Averno (AV), the amplitude of the vertical displacement shows a value of about 10 cm; then, between September 2020 and July 2021, the maximum uplift is about 13 cm in the area of

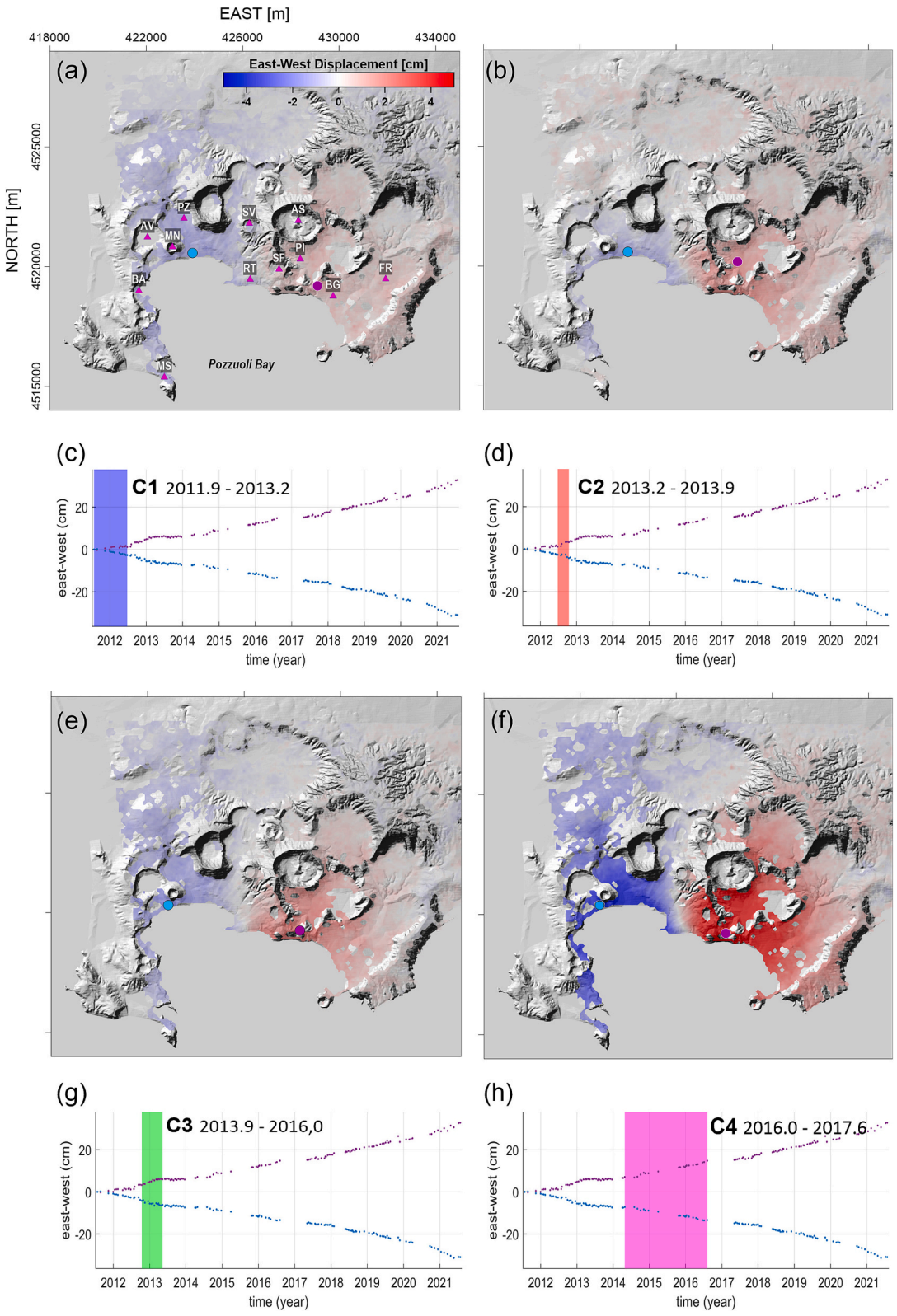

Fig. 5. DInSAR EW horizontal displacement maps, superimposed on the shaded relief map of SRTM-DEM, for the first four time intervals (C1: 2011.6–2012.5, C2: 2012.5–2012.8, C3:2012.8–2013.3, C4:2014.3–2016.6), identified by the TLA algorithm. These maps were derived by combining CSK ascending and descending orbits. (a) EW horizontal displacement map for the C1 time interval; (b) EW horizontal displacement map for the C2 time interval; (e) EW horizontal displacement map for the C3 time interval; (f) EW horizontal displacement map for the C4 time interval. In (c, d, g, h), the EW horizontal time series and the identified linear time intervals with different colors are reported. The blue and the purple dots in each map represent the pixels of the East and West time series. Positive and negative deformation values represent deformation movement toward East and West, respectively. (For interpretation of the references to colour in this figure legend, the reader is referred to the web version of this article.)

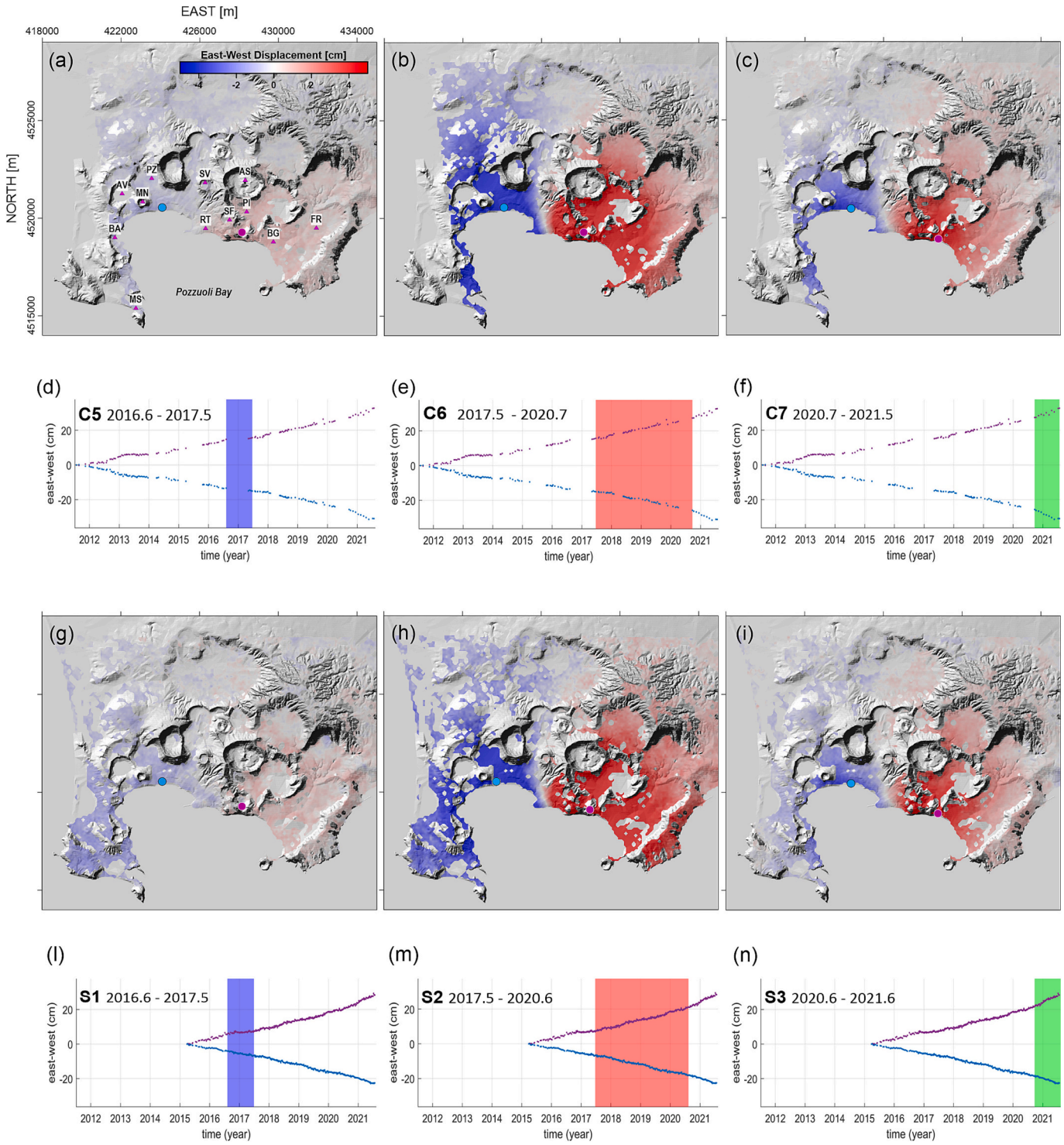

Fig. 6. DInSAR EW horizontal displacement maps, superimposed on shaded relief map of SRTM-DEM, for the following three time intervals: C5: 2016.7–2017.6, C6: 2017.8–2020.5, C7:2020.6–2021.6 and S1: 2016.7–2017.6, S2: 2017.8–2020.5, S3:2020.6–2021.6, identified by the TLA algorithm. These maps were derived by combining CSK ascending and descending orbits for C5, C6 and C7 time intervals and S-1 ascending and descending orbits for S1, S2 and S3 time intervals. (a) EW horizontal displacement map for the C5 time interval; (b) EW horizontal displacement map for the C6 time interval; (c) EW horizontal displacement map for the C7 time interval; (g) EW horizontal displacement map for the S1 time interval; (h) EW horizontal displacement map for the S2 time interval; (i) EW horizontal displacement map for the S3 time interval. In (d, e, f), the EW horizontal time series and the identified linear time intervals with different colors are reported in (l, m, n), as for (d, e, f) but for the S-1 EW horizontal time series component. The blue and the purple dots in each map represent the pixels of the East and West time series. Positive and negative deformation values represent deformation movement toward East and West, respectively. (For interpretation of the references to colour in this figure legend, the reader is referred to the web version of this article.)

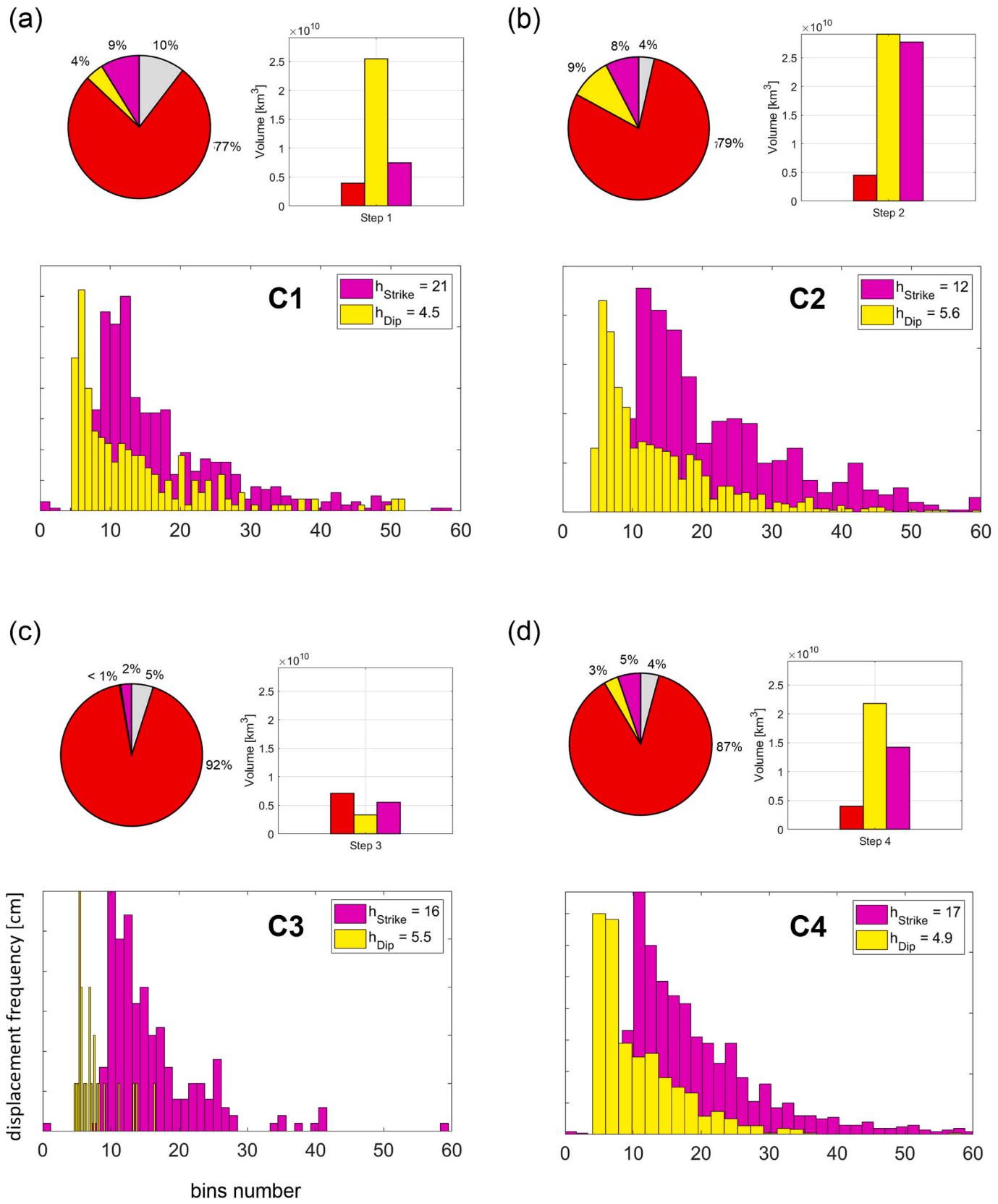

Fig. 7. Cell aggregation inverse model statistics relevant to the four identified time intervals (C1–C2–C3–C4). For each time step: the pie chart shows the percentage of activated cell during the inversion process, in that interval, by mechanism; the bar plot in the upper-right section show the volume affected by each mechanism; the histogram plot represents the distribution of the displacement for the dip-slip and the strike-slip solution and their mode value.

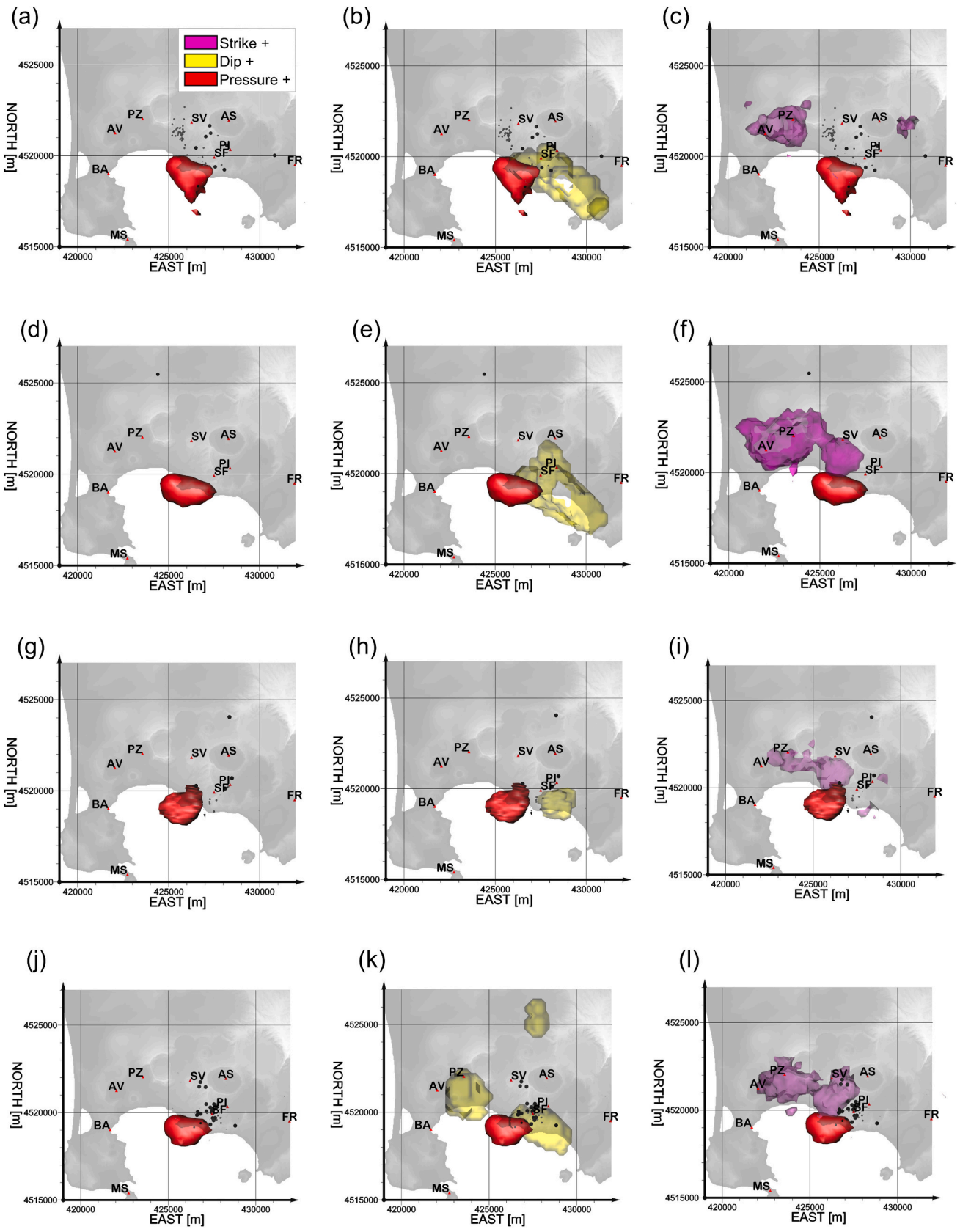

Fig. 8. Model Results. In panels (a, b, c), the aggregated model solutions for the first-time step (C1) are reported; in red is the rendering of the positive overpressure source, in yellow is the rendering of the positive dip-slip one and in magenta the rendering of the positive strike-slip one. In the panels groups (d, e, f), (g, h, i) and (j, k, l) as in previous panels, but for the second (C2), third (C3) and fourth (C4) time intervals, respectively. The black and grey spheres represent the seismicity during the considered period. (For interpretation of the references to colour in this figure legend, the reader is referred to the web version of this article.)

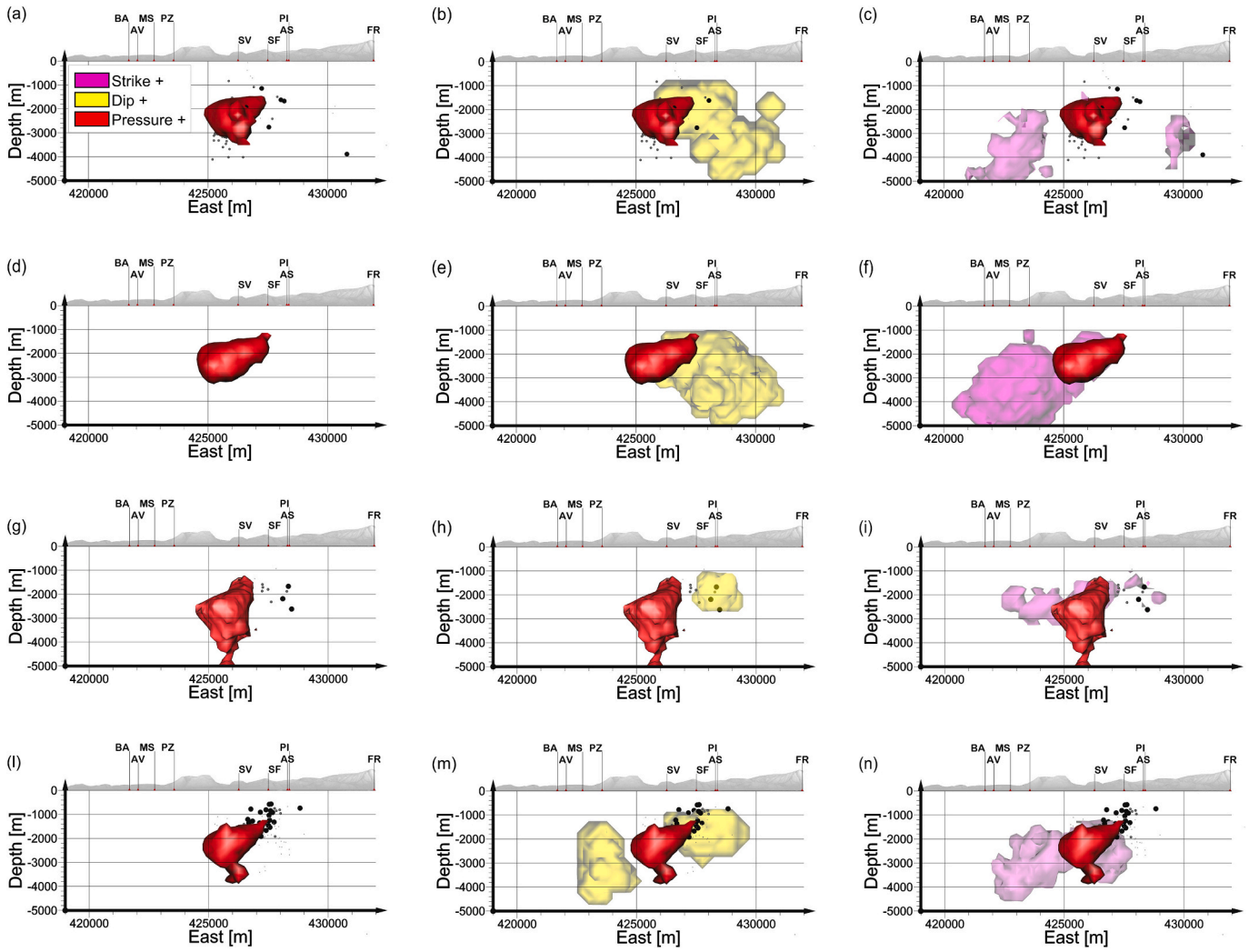

Fig. 9. Model Results. W-E vision of the model solutions reported in Fig. 8. Panels (a, b, c) for the C1 period, (d, e, f) for the C2 period, (g, h, i) for the C3 period and (l, m, n) for the C4 period. Panels a, d, g and l show only the pressure source. Panels b, e, h, and m show the pressure and dip-slip sources. Panels c, f, i and n are the pressure and strike-slip sources. The black and grey spheres represent the seismicity during the considered period.

Pozzuoli harbor (Fig. 4c, i). The computed vertical displacement maps (Fig. 4a, b, c, g, h, i) highlight that the geometry of the ground deformation pattern is characterized by an asymmetric distribution of the ground displacements concerning the maximum uplift signal, localized in the area of the Pozzuoli harbor (Pepe et al., 2019; Castaldo et al., 2021). In particular, the deformation signal affects a broad area at the western sector of the caldera and along the coast, reaching, during its maximum extension (C6-S2), the Baia town (BA) and Capo Miseno sites (MS). Instead, at the east of the maximum deformation region (the area comprised the Solfatara (SF), Pisciarelli (PI), and along the coast east of Pozzuoli Harbor (PH)), the vertical displacements decay very quickly and only partially affect the Fuorigrotta Plain (FR), with about 5 cm of vertical displacements during the maximum uplift episode (C6-S2 Interval), as also highlighted by Pepe et al. (2019). In this context, the spatial-temporal analysis of the SAR displacement maps revealed that most uplift signals appear to be constrained during the maximum intensity of the ground deformation by the presence of outcropping caldera floor structures (Bevilacqua et al., 2022; Vitale and Natale, 2023). This is well highlighted by the comparison between ground deformation and the structural map of the caldera region (Fig. 4b, h).

Figs. 5 and 6 show the EW components of the ground deformation in the 2011–2022 time window. During the C6-S2 interval, the horizontal displacement toward the east is about 12 cm in the area among Solfatara (SF), Pisciarelli (PI) and Bagnoli (BG), and about 10 cm toward the west close to Mt. Nuovo (MN). During the C7-S3 interval, the areas affected by the main horizontal displacements are the same as the C6-S2 interval but with lower intensity: about 6 cm toward the east and about 5 cm toward the west.

The EW component shows a slight asymmetry of the ground deformation pattern, with displacements with higher values in the eastern caldera region (Fig. 5f; Fig. 6b, c, h, i).

3.2. Model results

We modelled the VFS beneath CFc via cell sources aggregation (i.e., type, location, evolution, and nature), responsible for the observed ground deformation between 2011 and 2022. The results of the joint inversion of ascending and descending LOS for both sensors allow us to identify the 3D deformation sources as cell aggregations of different nature or type (e.g., pressure change, strike-slip, dip-slip), estimating magnitude values, position, geometry and temporal evolution. No tensile-model solution, that was able to fit the LOS data, was found. Figs. 8–10 show the achieved results during the four linear intervals (C1, C2, C3, C4), covering the 2011–2016 period.

Fig. 7 presents the statistical analysis performed on model solutions for each interval. The reported pie charts represent the overall volume

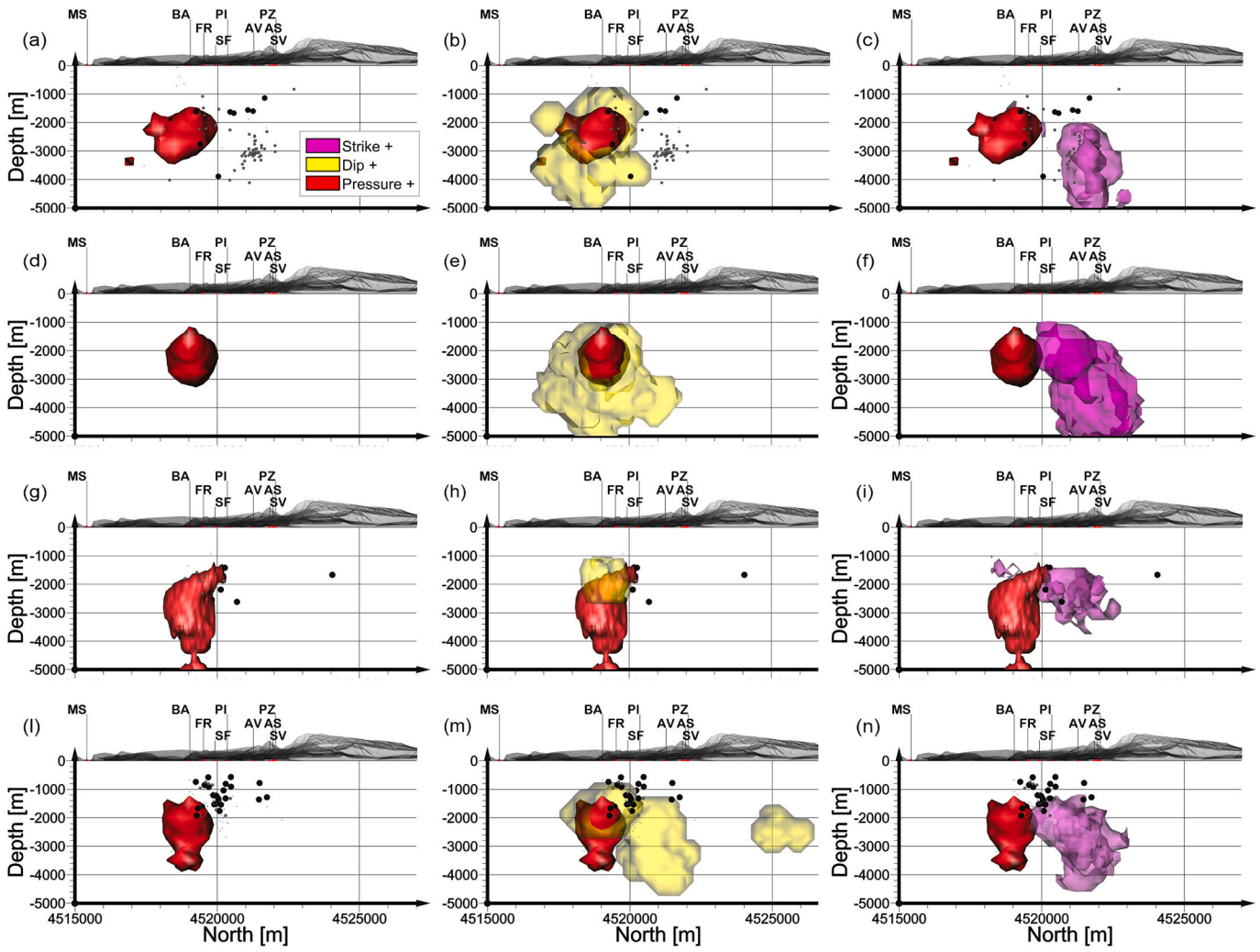

Fig. 10. Model Results. S-N vision of the model solutions reported in Fig. 8. Panels (a, b, c) for the C1 period, (d, e, f) for the C2 period, (g, h, i) for the C3 period and (l, m, n) for the C4 period. Panels a, d, g and l show only the pressure source. Panels b, e, h, and m show the pressure and dip-slip sources. Panels c, f, i and n are the pressure and strike-slip sources. The black and grey spheres represent the seismicity during the considered period.

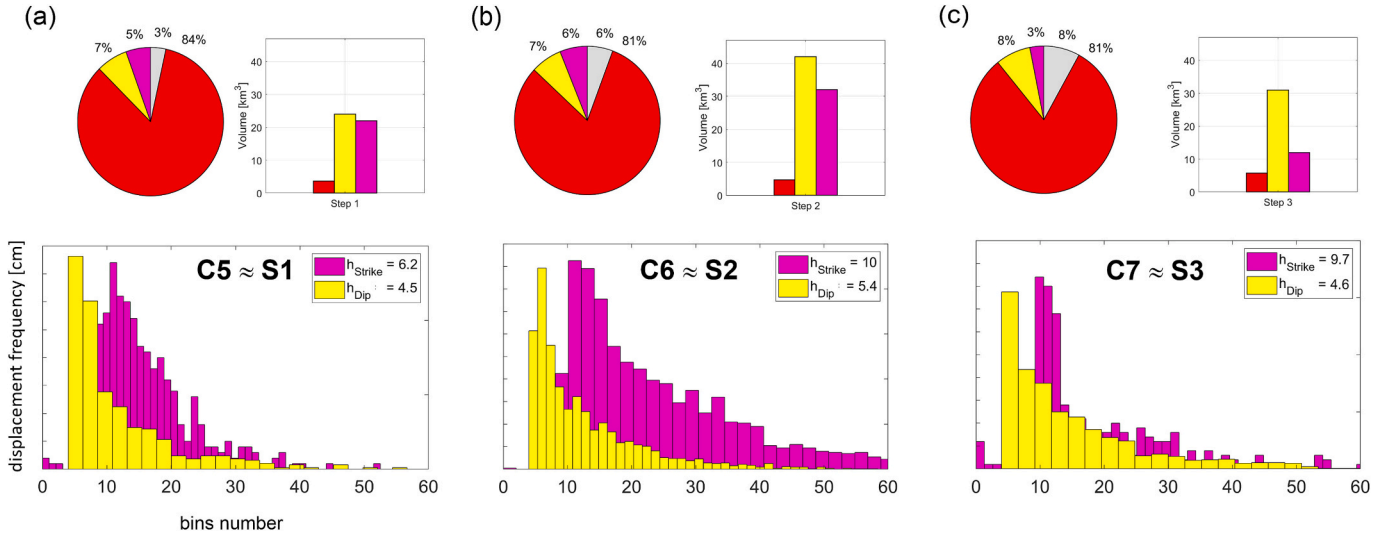

Fig. 11. Cell aggregation inverse model statistics relevant to the three identified time intervals (C5–C6–C7). For each time step: the pie chart shows the percentage of activated cell during the inversion process, in that interval, by mechanism; the bar plot in the upper-right section show the volume affected by each mechanism; the histogram plot represents the distribution of the displacement for the dip-slip and the strike-slip solution and their mode value.

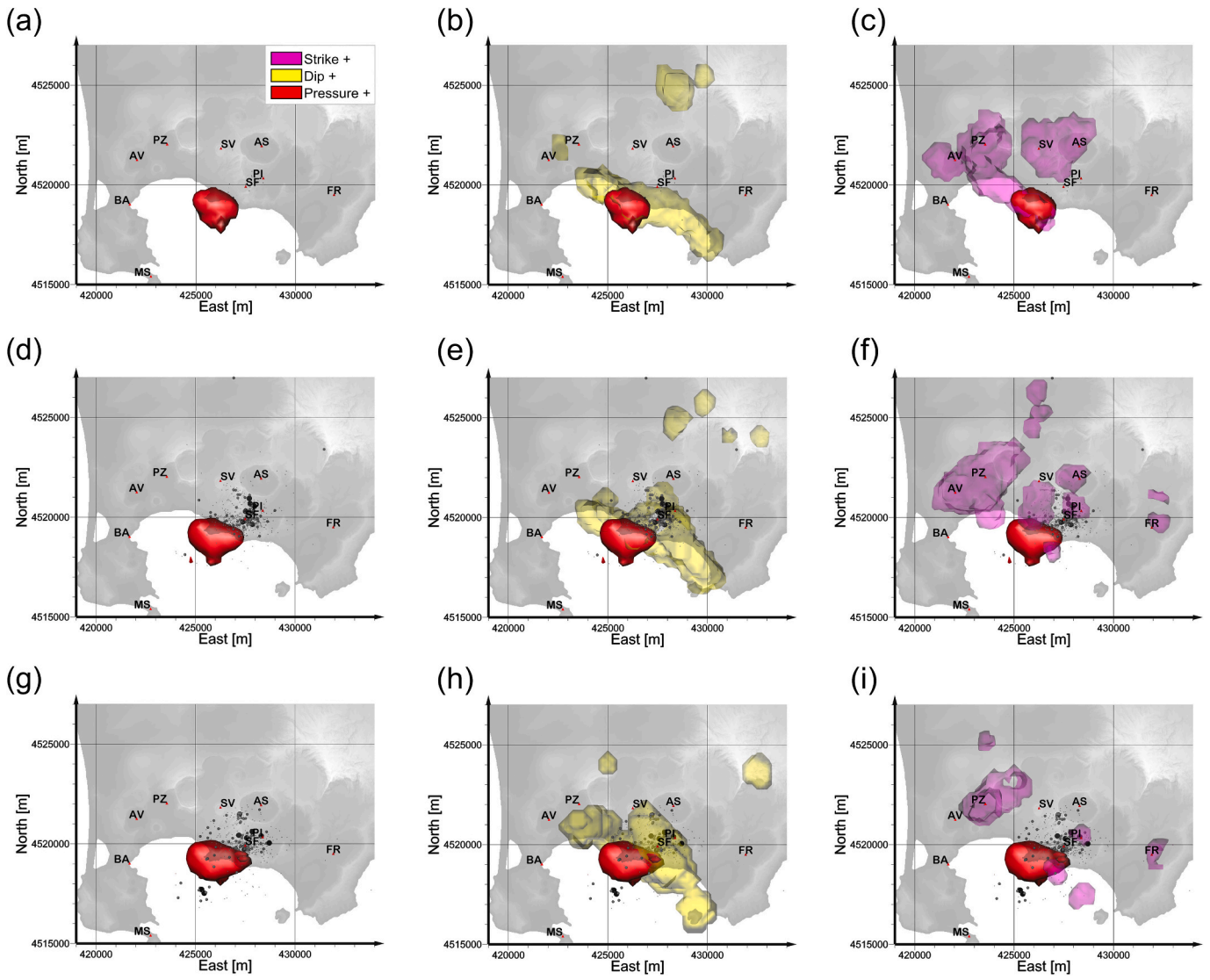

Fig. 12. Model Results. In panels (a, b, c), the aggregated model solutions for the C5 ≈ S1 time interval are reported; in red is the rendering of the positive overpressure source, in yellow is the rendering of the positive dip-slip one and in magenta the rendering of the positive strike-slip one. In the panels groups (d, e, f), (g, h, i) and (j, k, l) as in previous panels, for the C6 ≈ S2 and C7 ≈ S3 time intervals, respectively. The black and grey spheres represent the seismicity during the considered period. (For interpretation of the references to colour in this figure legend, the reader is referred to the web version of this article.)

per source mechanism's inversion results. In detail, for the C1 interval, the positive pressure solution represents 77 % of the total mechanisms; this tendency is also confirmed for the subsequent periods (C2), with a percentage of 79 %. Instead, for what concerns the dip and strike sources distribution, a percentage around 7–20 % is found for all considered time intervals. The negative model solutions for each modelled source are statistically irrelevant (less than 10 %). The frequency distributions for dip and strike type mechanisms emphasize the unimodality behavior and no-gaussian features of all model solutions. We use the "mode value" as a statistical indicator of the cell source distribution to select the source isosurface value that better represents the physical active process. Bar plots in Fig. 7a, b, c, d represent the total volume of each modelled mechanism. Regarding the overpressure solutions, we consider a strength threshold value of 55 MPa; this value represents the frictional mean crustal resistance that the pressure source has to overcome so that the deformation on the surface is detectable (Sibson, 1974). This threshold is obtained using the deviatoric stress value, $(\sigma_1 - \sigma_3) = \beta(\rho g z)(1 - \lambda)$ computed using the brittle equation (Sibson, 1974), where σ_1 and σ_3 are respectively maximum and minimum stress direction of the stress tensor; ρ is the average density value of the intra-caldera tuffs succession (2.4 g/cm^3) (Cubellis et al., 1995; Rosi and Sbrana, 1987); z is the estimated source bottom (~3 km b.s.l.), which is also the bottom of clustered natural seismicity (Fig. 1a); λ is the pore fluid factor and β is the parameter that depends on the fault type (3.0, 1.2 and 0.75 for thrust, strike-slip and normal faulting, respectively). We selected beta value of 0.75, which is the representative of the extensional stress regime at CFc (see focal mechanisms in Castaldo et al., 2019). A systematic increase of the overpressure volume from 4.3 km^3 to 6 km^3 is found: the volume growth rate from the C1 interval to the C3 Interval is about 30 %.

We show the achieved model results in terms of the spatial distribution of aggregated best fit source. The C1 and C2 overpressure sources are located in a region between the land coast and Pozzuoli Bay (Fig. 8a, d), elongated in the WNW-ESE direction, with a vertical extension that ranges between 1 and 3 km depth (Figs. 9a, d, 10a, d).

This source planar orientation is less evident for interval C3, where a more compact and elongated geometry reaches about 5 km depth (Fig. 8g). In the subsequent C4 interval, a renewed lateral spreading of the overpressure source is observed. In comparison, the model source depth arises at about 4 km (Fig. 8j).

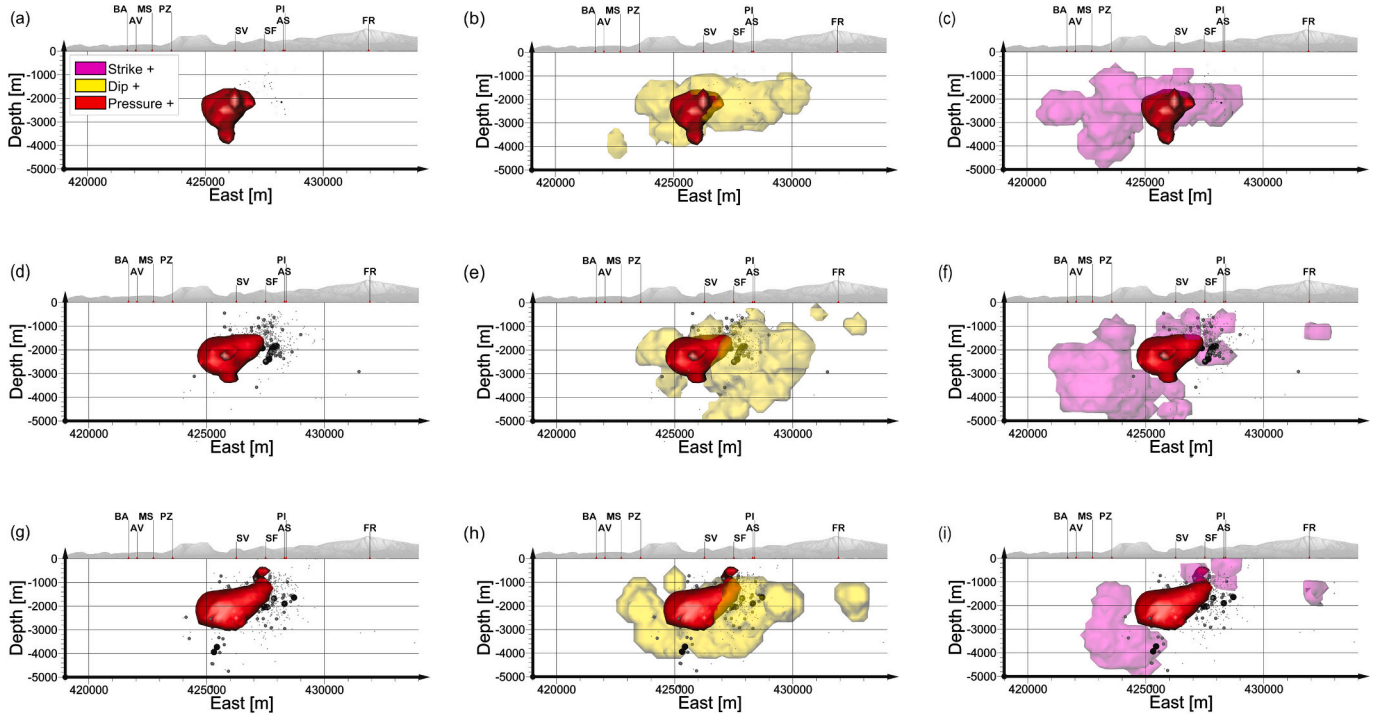

Fig. 13. Model Results. W-E vision of the model solutions reported in Fig. 11. Panels (a, b, c) for the C5 ≈ S1 time interval, (d, e, f) for the C6 ≈ S2 time interval, and (g, h, i) for the C7 ≈ S7 time interval. The black and grey spheres represent the seismicity localized during the considered period.

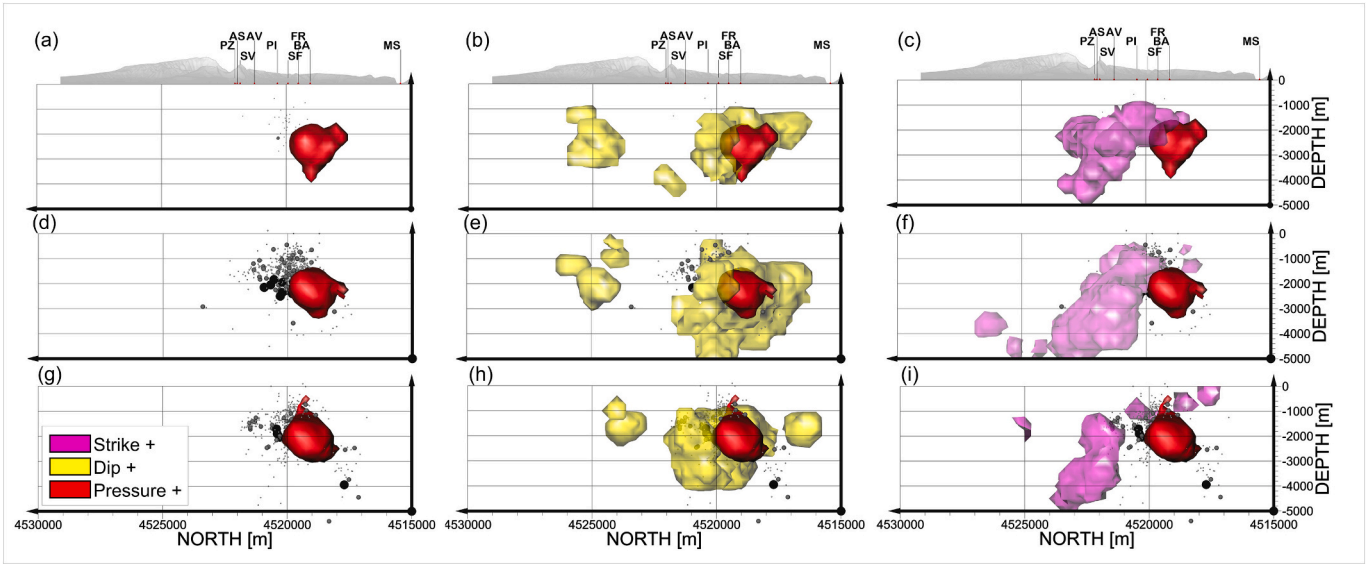

Fig. 14. Model Results. N-S vision of the model solutions reported in Fig. 11. Panels (a, b, c) for the C5 ≈ S1 time interval, (d, e, f) for the C6 ≈ S2 time interval, and (g, h, i) for the C7 ≈ S7 time interval. The black and grey spheres represent the seismicity localized during the considered period.

Concerning the modelled dip-slip regions (Fig. 8b, e), the main cluster is characterized by a WNW-ESE alignment. In comparison, in the subsequent C3 step (Fig. 8h), this region is reduced significantly near the overpressure source in the cluster region east of PI and SF sites. Finally, during the C4 interval (Fig. 8k), two new clustered regions were located in the Pozzuoli area and the northern part of the caldera. The vertical extension of modelled dip-slip regions ranges from 2 to 5 km of depth during the C1 interval (Figs. 9b, 10b), while during the C2 interval, the main cluster is included in a narrow volume localized from 1 to 3 km depth (Fig. 9m, 10m).

For the crustal regions affected by the strike-type mechanism, the model reveals the crustal volume of the caldera characterized by intense fracturing in the north-western region (Fig. 8c, f, i, l). The planimetric distribution of this mechanism shows a main cluster located between PZ and AV (Fig. 8c), from 1 to 4 km depth, during the C1 interval. The strike-type mechanism grows during the C2 interval, reaching the SV and SF sites (Fig. 8f); in this step, a major crustal region is involved, from 1 to 5 km depth. During the C3 interval, similarly to the dip-slip areas, a substantial reduction of strike-type mechanism volume is found (Figs. 8i, 9i, 10i). Finally, in the last interval, C4 (Figs. 8l, 9n, 10n), similar conditions of the C2 interval were found.

In Figs. 12–14, we show the achieved model results relevant to the

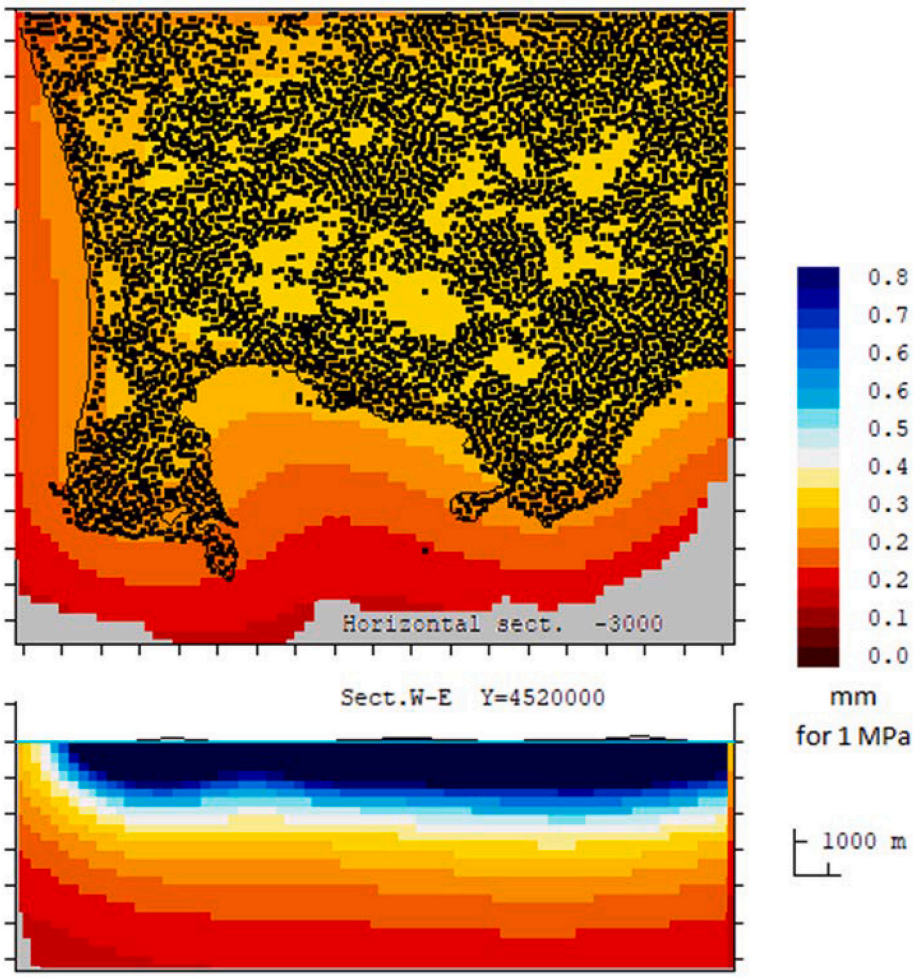

Fig. 15. Sensitivity values of the 3D adjusted model for the model pressure values of the deformation sources. Values in mm of ground deformation for a pressure change of 1 MPa and for a model volume of 1 km^3. Sensitivity decreases toward peripheral and deep regions. A similar pattern is deduced for sensitivity to other model strength values (dislocation values).

common satellite intervals, in which our performed TLA has revealed the presence of three linear intervals (C5/S1, C6/S2, C7/S3) that covered the 2016–2022 period for the which we apply the same statistical approach introduced in the previous step analysis (Fig. 11).

The estimated overpressure source is located in a region between the land coast and Pozzuoli Bay (Fig. 12a, d, g), elongated in the WNW-ESE direction. Specifically, its temporal evolution is characterized by spatial migration and growth of source volumes: an upward positive overpressure region migration is found, going from 4 km to 1.6 km of depth for C5/S1, to 3 km for C6/S2 and less than 1 km for C7/S3, with a localized increase of overpressure region that reaches 400 m b.s.l beneath the SF-PI area (Figs. 13a, d, g; 14a, d, g). Furthermore, moving from C5/S1 to C7/S3, a lateral spreading of the source can be observed, progressively involving more on-land regions (Figs. 12a, d, g; 13a, d, g; 14a, d, g). Specifically, the main cluster is characterized by a WNW-ESE alignment, which progressively evolves and affects internal areas such as SF, PI and SV (Fig. 12b, e, h). Two other clusters evolve, gradually involving the area between PZ, AV, and the coast. These cluster variations at depth are found between 1 and 4 km, surrounding the correspondent pressure source (Figs. 13b, e, h; 14b. e, h). The isosurface refers to the crustal regions characterized by a modelled upward slip of approximately 5 cm. Regarding the crustal areas affected by the strike-type mechanism, the model reveals regions with intense fracturing in the north-western area (Fig. 12c, f, i). The planimetric distribution of this mechanism shows two main clusters: the first is located between PZ and AV, with a depth from 1 to 5 km for C5/S1 interval, and the second is located in the SF-PI-SV area, with a depth from 1 km to 3 km for C6/S2, and from 1 km to the surface for C7/S3 (Figs. 13c, f, i; 14c, f, i).

As done in previous applications of this inversion methodology (Camacho et al., 2020; Fernández et al., 2021, 2022, 2024) we compute a 3D sensitivity analysis to estimate the reliability of the solutions (see Fig. 15) and compute the residuals between observed and computed deformation values (see Fig. 16). Fig. 15 can serve as a lower limit for the sensitivity and Fig. 16 as an upper limit for the residual estimation.

3.3. Discussion

Interpreting the source of deformation at Campi Flegrei has sparked vigorous debate among geoscientists, drawing upon a wide array of methodologies including geodetic analyses. While some researchers advocate for a magmatic origin, positing the movement of magma beneath the surface as the primary cause of deformation, others propose a hydrothermal explanation, suggesting that fluid migration and pressure changes within the hydrothermal system are driving factors. This debate has been enriched by contributions from studies such as those by Chiodini et al. (2017), leveraging geodetic sources to bolster the hydrothermal model, highlighting the pivotal role of fluid dynamics in shaping deformation patterns. Conversely, investigations by De Martino et al. (2021), building upon geodetic datasets, argue for a magmatic interpretation, emphasizing the presence of shallow magma chambers

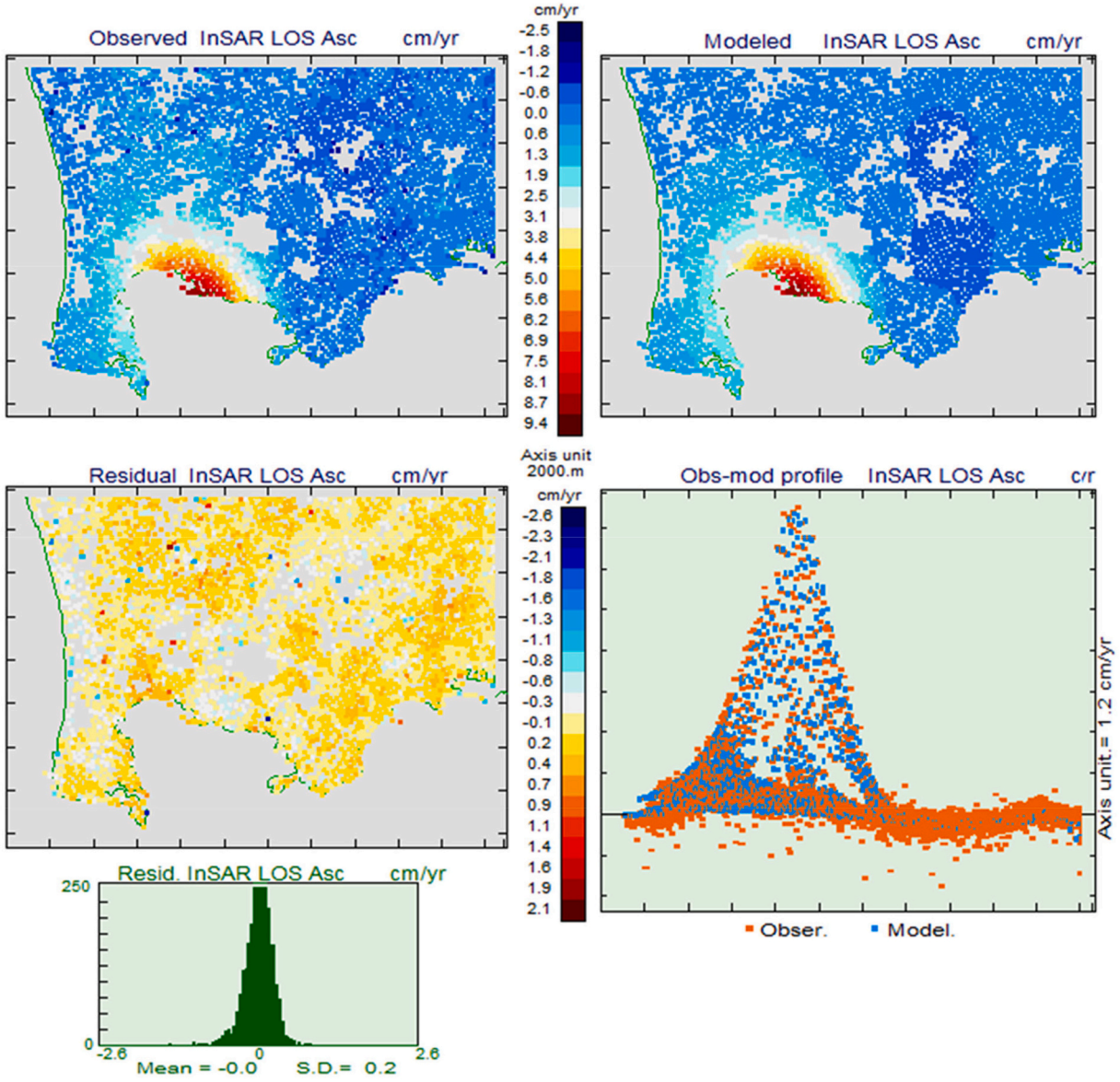

Fig. 16. An example of data fit for the ground deformation 3D modelling. It corresponds to the LOS Ascending component for 2020. Observed (after the calculation of rate values for date 2020), modelled and residual values (with a standard deviation of 0.2 cm/yr). Values correspond to deformation rate cm/yr. Similar for other descending component and other dates.

beneath the Campi Flegrei caldera. Additionally, pioneering work by Orsi et al. (1999), incorporating geodetic analyses, have provided crucial insights into the complex magmatic and hydrothermal processes operating within the caldera.

From multiplatform and multi-orbits InSAR data analysis it was possible to identify active structural features of CFc. Specifically, we find in the NW region of the caldera floor, a series of subparallel structures located between the Averno crater (AV) and San Vito (SV), with an ENE-WSW direction (Fig. 1a). NE of the caldera, the ground deformation field is constrained by a structure that extends from San Vito (SV) to the area of Pisciarelli (PI) along the external edge of Astroni (AS); instead, to the SE direction, the deformation signal is limited along the coast in a region located at SW with respect to the morphologic relief formed by the external quaquaversal of the Agnano crater and Mt. Spina, which border the Fuorigrotta plain (FR) from west to north. As mentioned above, the caldera region SW of the maximum uplift area experienced an uplift phenomenon, with intensities comparable to those of Fuorigrotta (FR), along the coastal region going from Averno crater (AV), Baia town (BA) to Capo Miseno (MS), during the most intense unrest phenomena intervals (Fig. 4b, h).

The 4D imaging of the VFS at CFc, achieved by modelling multi-platform SAR data, revealed a spatial evolution of the overpressure aggregate source over the 2011–2022 time interval. In particular, the source geometry in 2017 (C5/S1 interval) highlights the presence of a narrow funnel between 3 and 4 km depth in the bottom region of the source model (Figs. 13a; 14a), which can be interpreted as the main magma alimentation channel (Wohletz et al., 1999; D'Auria et al., 2015; Castaldo et al., 2019). This feature agrees with the source geometry detected during the previous model steps C3 and C4 (Fig. 9g, l).

During the C6/S2 (2018–2020) interval, a lateral spreading process of the pressurized source is found. Specifically, this evolution trend is evident moving from the C5/S1 interval to the C6/S2 interval. We interpreted this as an extended region where, according to previous works, a multiphase pressurized fluid occurs (Siniscalchi et al., 2019).

As already mentioned, this phenomenon produces a WNW-ESE source growing, in good agreement with previous works (Samsonov et al., 2014; D'Auria et al., 2015; Castaldo et al., 2021), coupled with increasing seismicity localized in the shallowest part of the overpressure

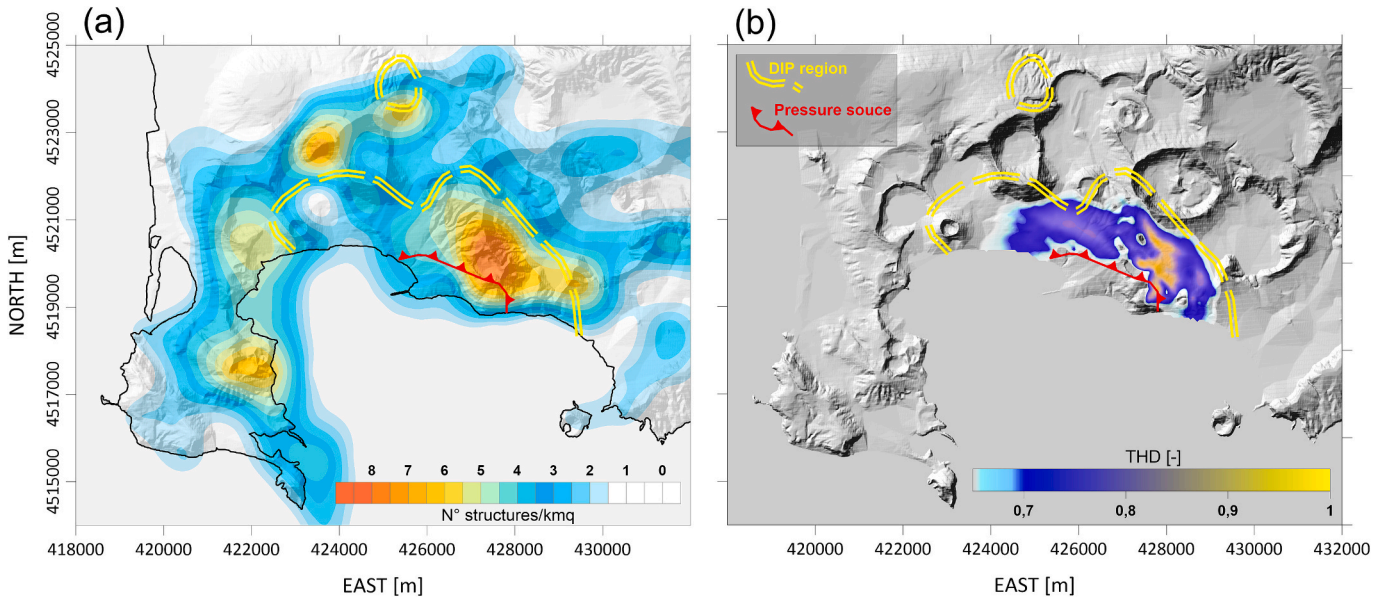

Fig. 17. Model Validation. (a) The density distribution map computed by the structural lineaments map of Fig. 1a, superimposed on the shaded relief map of SRTM-DEM of CFc. (b) Normalized THDw map relevant to the third time interval, superimposed on the shaded relief map of SRTM-DEM. The red and yellow lines represent the surface projection of the overpressure source and the dip-slip region for the third time interval. (For interpretation of the references to colour in this figure legend, the reader is referred to the web version of this article.)

source (Figs. 12d, g; 13d, g; 14d, g); this could indicate the ascent of a new batch of magma. The modelled dip-slip areas show the same planimetric orientation of the overpressure distribution and may reflect crustal fracturing associated with the magma input from deeper areas. The lateral migration (source spreading phenomena) also continues during the C7/S3 (2021−2022) interval, where a narrow conduit-like overpressure source reaches a depth of about 400 m beneath the SF-PI area. Fig. 13g shows the source bottom from 4 to 3 km. A low-magnitude seismicity cluster also surrounds the shallowest part of the overpressure source.

To verify the robustness and validity of the achieved results, we carried out three post-processing analyses, which can be summarized as follows: (i) A comparison between the dip-slip region modelled in the C7/S3 interval and the density distribution map of the outcropping structures (Fig. 17a), highlighting that the modelled dip-slip region identifies an area between the external perimeter of the overpressure source (red body in Fig. 17a) and the region that shows the highest density values of the distribution of the outcropping structure.

(ii) A comparison between the modelled dip-slip region for the C7/S3 period and the normalized THD_w distribution (see methods section) computed on the cumulative vertical displacement of the same time interval. The THD_w maxima, which indicates the projection at the ground of displacement source boundaries and/or the presence of structural heterogeneity, perfectly falls in the area between the model dip region and the overpressure source border (Fig. 17b). The achieved results confirm the capability of our approach to identify highly fractured regions of the caldera that are not strictly associated with the dynamics of the VFS source. In particular, the modelled dip-slip sources distribution can be interpreted as an area where the ground deformation field is modulated by the presence of the structural lineaments, affecting the intra-caldera tuffs successions (Bevilacqua et al., 2015).

(iii) A 3D spatial distribution of principal stress direction derived by FE forward model in a structural mechanics context, using the overpressure region active during the C7/S3 interval as the source. According to the Anderson theory of the reactivation fault, the model results (Fig. 18) highlight that the perturbative effects, induced by an overpressure source, are limited to the internal region of the CFc and laterally decay exponentially from the source perimeter to below 3 km depth. The distribution of the stress tensor in the plain XY is radial, with the maximum main axis (σ_1) having a circumferential trend; the intermediate main axis (σ_2) has a radial trend, while the minimum main axis (σ_3) systematically shows a vertical orientation (Z). In particular, at a depth of 1 km, the σ_2 axis is tensional along the perimeter of the source, after which it transforms into a compressional one, decaying then rapidly moving away from the source. Instead, at depths of 2–3 km, the σ_2 axis is always compressive, and it decays quickly as the distance from the source increases. Our analysis reveals that the spatial orientation of the main stress axes is compatible with a portion of the crust, between 2 and 3 km depth, characterized by dip dislocation, as predicted by our 3D tomographic inversion model. This spatial-stress orientation is also in good agreement with the distribution of computed Von Mises stress (Fig. 18b), which emphasizes the anisotropy distribution of the mechanical failure in the crust. In particular, the spatial anisotropic orientation of the modelled source may justify the onset of a dip-slip region, confirmed by the existence of the dip-slip area in the performed geodetic imaging tomography.

4. Main conclusions

The 4-D tomographic geodetic inversion, performed via optimization of the multi-platform radar satellite data between 2011 and 2022, revealed an aggregate overpressure source that grows and systematically migrates toward the SF- PI region. In Fig. 19, we show a spatial and temporal integrated model for the optimized geodetic source, which includes the main processes that characterized the VPS evolution in the last decade.

The results show a narrow funnel zone, which may represent the active alimentation system, between 4 and 5 km depth (C3–C4 interval). Wohletz et al. (1999), D'Auria et al. (2015) and Castaldo et al. (2019) identified a magmatic source between 2 and 4 km depth by thermo-fluid dynamic modelling based on thermal and ground deformation data. Accordingly, we interpret the upper part of the funnel (about 3–4 km depth) as a partially melted lens. This region is located below an aggregate volume that extends from 3 to 1.5 km depth and is expanded laterally during the C5/S1-C6/S2 period. The overpressure source evolution, in terms of lateral spreading and the consequent formation of a very superficial broad overpressure region, is in good agreement with the anisotropic distribution of the EW horizontal component of the

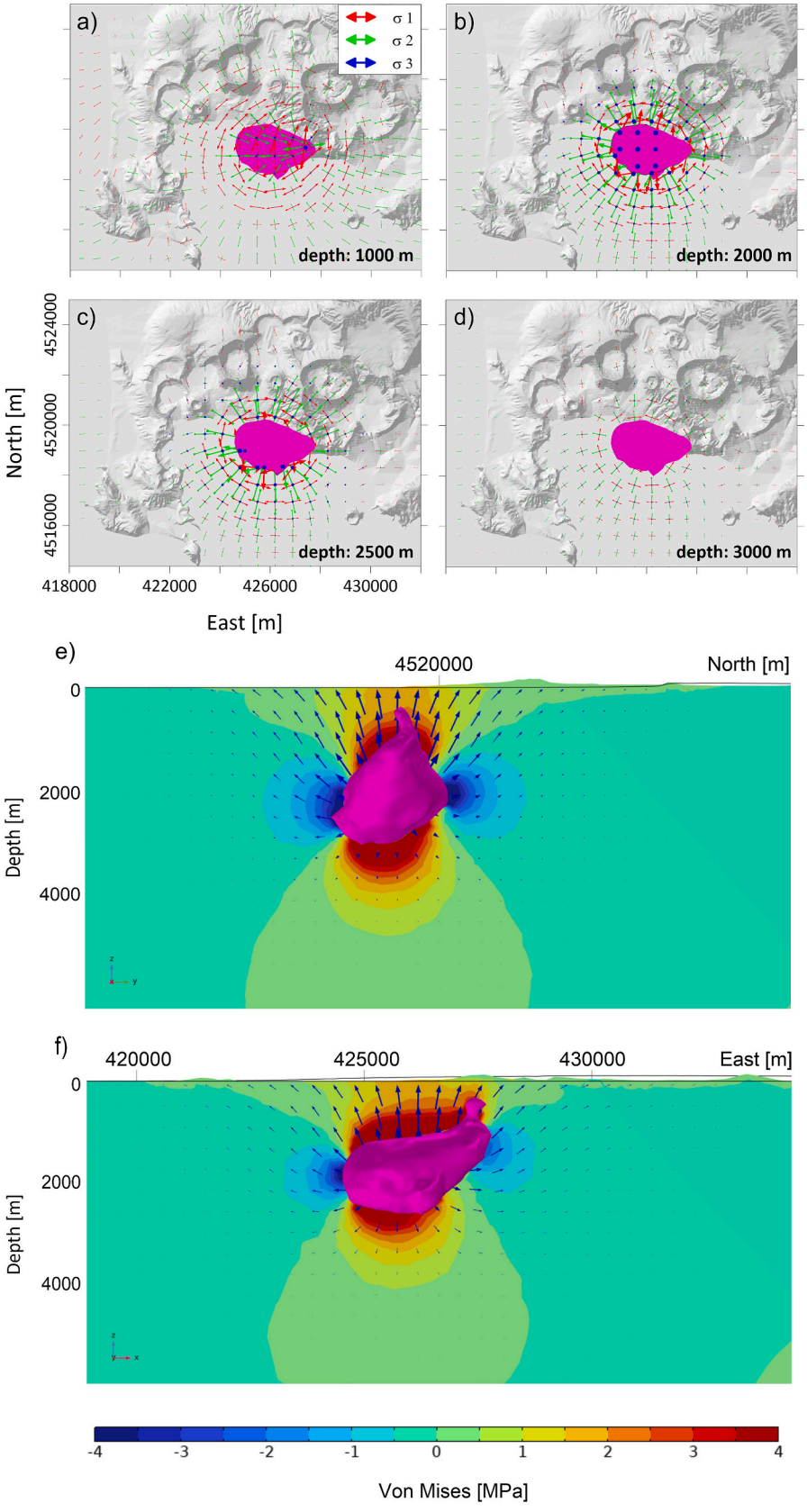

Fig. 18. Stress sources Model. (a–d) Structural mechanics FE model: principal stress axes orientation at different depths is reported. The magenta body represents the projection of the overpressure source, relevant to the last time interval, over the LANDSAT 8 optical image of the CFc. (e) EW and (f) NS view of von Mises stress changes. The blue arrow indicates the direction of the crustal modelled deformation field, and in magenta, the isosurface rendering of the computed overpressure source. (For interpretation of the references to colour in this figure legend, the reader is referred to the web version of this article.)

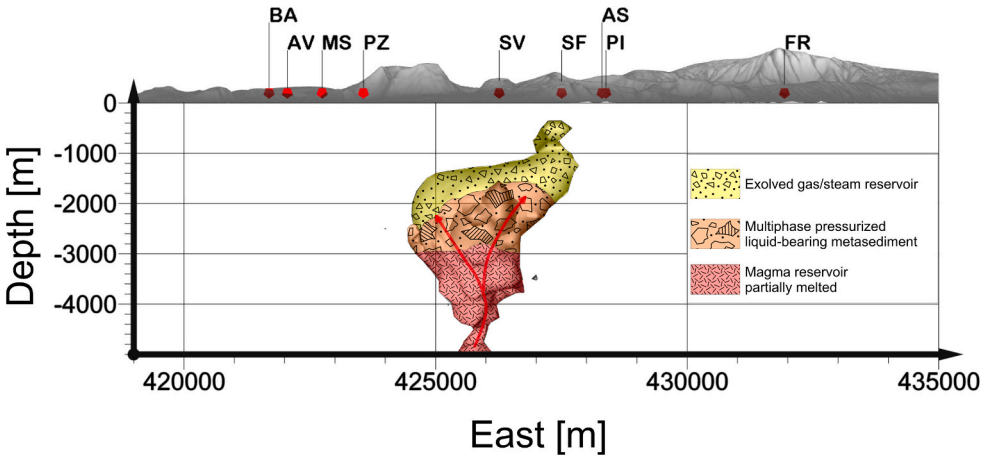

Fig. 19. VFS interpretation model of the 2011–2022 CFc tomographic inversion results. The yellow region represents the model source solution relevant to the C7 ≈ S3 TLA time interval; the orange region is derived from the C6 ≈ S2 time interval, while the red region is the fusion of the model result related to C3 to the C5 ≈ S1. The red arrows represent the migration and spreading process directions inside VFS. See also Figs. 9–14. (For interpretation of the references to colour in this figure legend, the reader is referred to the web version of this article.)

ground deformation pattern (Fig. 5; Fig. 6). We interpreted this lateral source spreading process over time as a region consisting of multiphase pressurized liquid-bearing metasediment (Fig. 8a, d, g, j; Figs. 9–10; Fig. 12a, d, g; Figs. 13–14). This area also has been identified as a possible thermo-poro-elastic source of deformation by Nespoli et al. (2023). The interpretative model also agrees with Siniscalchi et al. (2019), Castaldo et al. (2021) and Troiano et al. (2022).

According to Siniscalchi et al. (2019), within the first kilometer, the shallower aggregation region is interpreted as an exsolved gas/steam reservoir region. In particular, the analysis performed on the last time interval (C7/S3) highlighted the existence/onset of an overpressure region localized just below the PI and SF area at about 400 m of depth. This narrow region could represent the preferred gas pathway feeding the SF and PI fumaroles where more than 3500 t of CO_2 per day are recorded. The shallow funnel of the overpressure source is in good agreement with Troiano et al. (2022), which used high-resolution MT soundings to analyze the PI-SF area.

Our tomographic inversion model, characterized by the progressive growth of aggregated sources, provided a coherent image of the overpressure source and jointly identified the crustal regions that concentrate the surrounding stresses (i.e., dip and strike volume solutions). Accordingly, the computed stress field rapidly decays, moving away from the area of maximum uplift at a depth greater than 3 km that is in a good agreement with previous studies on the area (Wohletz et al., 1999; Trasatti et al., 2008; Amoruso et al., 2014; D'Auria et al., 2015; Castaldo et al., 2019; Castaldo et al., 2021).

In conclusion, our analysis reveals that the source responsible for the 2011–2022 observed ground deformation, and seismicity may be interpreted as a continuous spatial source. Indeed, the comparison of the computed 3D stress field changes and the seismicity emphasizes a good spatial fit between the location of maximum von Mises stress and the spatial clustering of the natural recorded events.

The available geophysical, geological/structural and petrophysical information reveals the presence of different vertically and laterally rheological conditions both at the passage caldera border (Castaldo et al., 2019). A rheological transition from magmatic to hydrothermal characteristics can be inferred from the deepest to the shallower part of the deformation body. For the VFS deeper region, the tomographic inversion results performed between 2011 and 2014 (Fig. 8a, d, g, j; Figs. 9–10) reveal an overall migration of the overpressure regions from 5 km up to 3 km depth. This migration appears to agree with the results achieved by D'Auria et al. (2015), which addressed the magmatic nature of the source to justify the 2012–2013 ground uplift episode, also in good agreement with the findings of Chiodini et al. (2015).

Another relevant aspect that derives from our results is the presence of a well correlated dip-slip region, which is localized with respect to the observed seismicity clusters (Fig. 8b, e, h, k; Figs. 9–10; Fig. 12b, e, h, k; Figs. 13–14). We emphasize that this intensely fractured region (modelled dip-slip volume) could favor the magma rising, also externally to the modelled overpressure plumbing systems; this represents a crucial element never previously considered.

Numerous studies support this modelled scenario. In fact, the processes of magma ascent are strongly influenced by the physical and mechanical properties of the crustal lithologies underlying the outcropping caldera region. The intense fracturing of subsurface caldera crustal units comprising alternating layers of compact tuff, marine/terrigenous sediments, and variably consolidated pyroclastics, may have played a crucial role in facilitating magma ascent and the concentration of hot fluids (Acocella et al., 2004), even outside the modelled overpressure plumbing systems region in sensu strictu (Figs. 19, 18). Similar phenomena have been observed in other calderas, such as Long Valley (Dvorak and Dzurisin, 1997), Taupo, and La Valles, where comparable lithological contrasts have facilitated magma migration (Cole et al., 2005; Kennedy et al., 2012).

For these reasons, we believe that the continuous analysis of the space-time source variations and associated stress field are key elements to identify phenomena that may precede future possible eruptive scenarios. This analysis may assist in defining hazard zonation scenarios, especially in the case of the polygenic volcanic field. In such cases the lack of spatial persistence of the eruptive vent poses a challenge in determine the future spatial location of the active volcanic magma pathways, and identifying of the most hazardous area.

Our study, using multi-platform InSAR deformation data of CFc volcanic area, along with a new state-of-the-art interpretation tool, allowed us to obtain new results on the acting sources (types, location and 3D shapes, as well as the time evolution of these characteristics) that would have been unattainable using classical observation and interpretation approaches. Similar conclusions were reached in studies examining Mt. Etna, Italy (Camacho et al., 2020), and the volcanic unrest in La Palma (Canary Islands, Spain) (Fernández et al., 2021) and its subsequent eruption (Fernández et al., 2022).

Computer codes

The 3D analysis of achieved model results, is performed using licensed commercial software from Golden Software, including Voxler and Surfer 16. Satellite data is processed with algorithms implemented in IDL and MATLAB, which are available upon request from the authors.

The 3D stress model was implemented in the COMSOL Multiphysics commercial package, and the source code can be obtained by contacting the authors. Defsour® software for inversion of LOS data (Fernández et al., 2022) is available under request to the authors using a transfer agreement, for volcano monitoring and research, excluding commercial applications.

CRediT authorship contribution statement

Pietro Tizzani: Writing – review & editing, Writing – original draft, Visualization, Validation, Supervision, Resources, Project administration, Methodology, Funding acquisition, Formal analysis, Conceptualization. **José Fernández:** Writing – review & editing, Writing – original draft, Supervision, Software, Resources, Project administration, Methodology, Investigation, Funding acquisition, Formal analysis, Conceptualization. **Andrea Vitale:** Software, Validation, Formal analysis, Investigation, Writing - Original Draft, Writing - Review & Editing, Visualization. **Joaquín Escayo:** Writing – review & editing, Visualization, Resources, Investigation, Formal analysis. **Andrea Barone:** Writing – review & editing, Writing – original draft, Visualization, Validation, Software, Investigation, Formal analysis. **Raffaele Castaldo:** Writing – review & editing, Writing – original draft, Methodology, Investigation, Funding acquisition. **Susi Pepe:** Writing – review & editing, Writing – original draft, Investigation, Data curation. **Vincenzo De Novellis:** Writing – review & editing, Writing – original draft, Visualization, Validation. **Giuseppe Solaro:** Writing – review & editing, Resources. **Antonio Pepe:** Writing – review & editing, Data curation. **Anna Tramelli:** Writing – review & editing, Methodology. **Zhongbo Hu:** Writing – review & editing. **Sergey V. Samsonov:** Writing – review & editing. **Isabel Vigo:** Writing – review & editing, Funding acquisition. **Kristy F. Tiampo:** Writing – review & editing. **Antonio G. Camacho:** Writing – review & editing, Validation, Software, Resources, Methodology, Investigation, Formal analysis, Data curation, Conceptualization.

Declaration of competing interest

The authors declare that they have no conflict of interest.

Data availability

Data sets related to this article can also be found at the digital. CSIC repository, http://hdl.handle.net/10261/341157.

Acknowledgements

This work has been supported by Spanish Agencia Estatal de Investigación (10.13039/501100011033) grant RTI2018-093874-B-I00 (DEEP-MAPS), and grants G2HOTSPOTS (PID2021-122142OB-I00) and Defsour-PLUS (PDC2022–133304-I00) from the AEI/10.13039/501100011033/Union Europea NextGeneration. We thank ASI (Italian Space Agency) Project “DInSAR - 3M” (ASI Contract n. 2021-8-U.0 “DInSAR Multi-frequency/Multi-platform for Multi-scale analysis of ground movements” to partially support the activities. We also thank the Italian DPC and DInSAR-3M projects for partially funding this research activity and ASI and ESA for providing the SAR images. The efforts of KFT were supported in part by NOAA cooperative agreements NA17OAR4320101 and NA22OAR4320151 and NSF Award OAC 1835566. This work represents a contribution to CSIC PTI TELEDETEC. We would like to express our sincere gratitude to Peppe Luongo for his valuable suggestions and insightful contributions to our discussions.

References

Acocella, V., Funiciello, R., Giordano, G., Neri, M., 2004. The role of extensional structures on magma ascent and caldera collapse. J. Volcanol. Geotherm. Res. 129, 199–217. https://doi.org/10.1016/S0377-0273(03)00240-3.

Amoruso, A., Crescentini, L., 2023. DInSAR data reveal an intriguing contemporaneous onset of deep deflation below Vesuvio and the ongoing Campi Flegrei uplift. Remote Sens. (Basel) 15, 3038. https://doi.org/10.3390/rs15123038.

Amoruso, A., Crescentini, L., Sabbetta, I., 2014. Paired deformation sources of the Campi Flegrei caldera (Italy) required by recent (1980–2010) deformation history. J. Geophys. Res. Solid Earth 119, 858–879. https://doi.org/10.1002/2013JB010392.

Anderssohn, J., Motagh, M., Walter, T.R., Rosenau, M., Kaufmann, H., Oncken, O., 2009. Surface deformation time series and source modeling for a volcanic complex system based on satellite wide swath and image mode interferometry: the Lazufre system, central Andes. Remote Sens. Environ. 113, 2062–2075. https://doi.org/10.1016/j.rse.2009.05.004.

Arab-Sedze, M., Heggy, E., Bretar, F., Berveiller, D., Jacquemoud, S., 2014. Quantification of L-band InSAR coherence over volcanic areas using LiDAR and in situ measurements. Remote Sens. Environ. 152, 202–216. https://doi.org/10.1016/j.rse.2014.06.011.

Barone, A., Pepe, A., Tizzani, P., Fedi, M., Castaldo, R., 2022a. New advances of the multiscale approach for the analyses of insar ground measurements: the yellowstone caldera case-study. Remote Sens. (Basel) 14, 5328. https://doi.org/10.3390/rs14215328.

Barone, A., Fedi, M., Pepe, S., Solaro, G., Tizzani, P., Castaldo, R., 2022b. Modeling the deformation sources in volcanic environments through multiscale analysis of DInSAR measurements. Front. Earth Sci. 10, 859479. https://doi.org/10.3389/feart.2022.859479.

Berardino, P., Fornaro, G., Lanari, R., Sansosti, E., 2002. A new algorithm for surface deformation monitoring based on small baseline differential SAR interferograms. IEEE Trans. Geosci. Remote Sens. 40, 2375–2383. https://doi.org/10.1109/TGRS.2002.803792.

Bevilacqua, A., Isaia, R., Neri, A., Vitale, S., Aspinall, W.P., Bisson, M., Flandoli, F., Baxter, P.J., Bertagnini, A., Esposti Ongaro, T., Iannuzzi, E., Pistolesi, M., Rosi, M., 2015. Quantifying volcanic hazard at Campi Flegrei caldera (Italy) with uncertainty assessment: I. Vent opening maps. J. Geophys. Res. 120, 2309–2329. https://doi.org/10.1002/2014JB011775.

Bevilacqua, A., De Martino, P., Giudicepietro, F., Ricciolino, P., Patra, A., Pitman, E.B., Bursik, M., Voight, B., Flandoli, F., Macedonio, G., Neri, A., 2022. Data analysis of the unsteadily accelerating GPS and seismic records at Campi Flegrei caldera from 2000 to 2020. Sci. Rep. 12, 19175. https://doi.org/10.1038/s41598-022-23628-5.

Blakely, J.R., 1996. Potential Theory in Gravity and Magnetic Applications. Cambridge University Press.

Bonaccorso, A., Cianetti, S., Giunchi, C., Trasatti, E., Bonafede, M., Boschi, E., 2005. Analytical and 3-D numerical modelling of Mt. Etna (Italy) volcano inflation. Geophys. J. Int. 163, 852–862. https://doi.org/10.1111/j.1365-246X.2005.02777.x.

Bonafede, M., Amoruso, A., Crescentini, L., Gottsmann, J.H., Todesco, M., Trasatti, E., 2022. Source modelling from ground deformation and gravity changes at the Campi Flegrei caldera, Italy. In: Orsi, G., D'Antonio, M., Civett, L. (Eds.), Campi Flegrei a Restless Caldera in a Densely Populated Area. Springer-Verlag GmbH Germany, pp. 283–309. https://doi.org/10.1007/978-3-642-37060-1_11.

Camacho, A.G., Fernández, J., 2019. Modelling 3D free-geometry volumetric sources associated to geological and anthropogenic hazards from space and terrestrial geodetic data. Remote Sens. (Basel) 11, 2042. https://doi.org/10.3390/rs11172042.

Camacho, A.G., González, P.J., Fernández, J., Berrino, G., 2011. Simultaneous inversion of surface deformation and gravity changes by means of extended bodies with a free geometry: application to deforming calderas. J. Geophys. Res. Solid Earth 116, B10401. https://doi.org/10.1029/2010JB008165.

Camacho, A.G., Fernández, J., Cannavó, F., 2018. PAF: a software tool to estimate free-geometry extended bodies of anomalous pressure from surface deformation data. Comput. Geosci. 111, 235–243. https://doi.org/10.1016/j.cageo.2017.11.014.

Camacho, A.G., Fernández, J., Samsonov, S.V., Tiampo, K.F., Palano, M., 2020. Multisource 3D modelling of elastic volcanic ground deformations. Earth Planet. Sci. Lett. 547, 116445. https://doi.org/10.1016/j.epsl.2020.116445.

Cannavò, F., Camacho, A.G., González, P.J., Mattia, M., Puglisi, G., Fernández, J., 2015. Real time tracking of magmatic intrusions by means of ground deformation modeling during volcanic crises. Sci. Rep. 5, 10970. https://doi.org/10.1038/srep10970.

Castaldo, R., D'Auria, L., Pepe, S., Solaro, G., De Novellis, V., Tizzani, P., 2019. The impact of crustal rheology on natural seismicity: Campi Flegrei caldera case study. Geosci. Front. 10, 453–466. https://doi.org/10.1016/j.gsf.2018.02.003.

Castaldo, R., Tizzani, P., Solaro, G., 2021. Inflating source imaging and stress/strain field analysis at Campi Flegrei caldera: the 2009–2013 unrest episode. Remote Sens. (Basel) 13, 2298. https://doi.org/10.3390/rs13122298.

Cella, F., Fedi, M., 2015. High-resolution geophysical 3D imaging for archaeology by magnetic and EM data: the case of the iron age settlement of Torre Galli, southern Italy. Surv. Geophys. 36, 831–850. https://doi.org/10.1007/s10712-015-9341-3.

Charlton, D., Kilburn, C., Edwards, S., 2020. Volcanic unrest scenarios and impact assessment at Campi Flegrei caldera, Southern Italy. J. Appl. Volcanol. 9, 7. https://doi.org/10.1186/s13617-020-00097-x.

Chen, Y., Remy, D., Froger, J.-L., Peltier, A., Villeneuve, N., Darrozes, J., Perfettini, H., Bonvalot, S., 2017. Long-term ground displacement observations using InSAR and GNSS at Piton de la Fournaise volcano between 2009 and 2014. Remote Sens. Environ. 194, 230–247. https://doi.org/10.1016/j.rse.2017.03.038.

Chiodini, G., Caliro, S., De Martino, P., Avino, R., Gherardi, F., 2012. Early signals of new volcanic unrest at Campi Flegrei caldera? Insights from geochemical data and physical simulations. Geology 40, 943–946. https://doi.org/10.1130/G33251.1.

Chiodini, G., Vandemeulebrouck, J., Caliro, S., D'Auria, L., De Martino, P., Mangiacapra, A., Petrillo, Z., 2015. Evidence of thermal-driven processes triggering

the 2005–2014 unrest at Campi Flegrei caldera. Earth Planet. Sci. Lett. 414, 58–67. https://doi.org/10.1016/j.epsl.2015.01.012.
Chiodini, G., Selva, J., Del Pezzo, E., Marsan, D., De Siena, L., D'auria, L., Bianco, F., Caliro, S., De Martino, P., Ricciolino, P., Petrillo, Z., 2017. Clues on the origin of post-2000 earthquakes at Campi Flegrei caldera (Italy). Sci. Rep. 7, 4472. https://doi.org/10.1038/s41598-017-04845-9.
Cole, J.W., Milner, D.M., Spinks, K.D., 2005. Calderas and caldera structures: a review. Earth-Sci. Rev. 69, 1–26. https://doi.org/10.1016/j.earscirev.2004.06.004.
Crozier, J., Karlstrom, L., Montgomery-Brown, E., Angarita, M., Cayol, V., Bato, M.G., Wang, T.A., Grapenthin, R., Shreve, T., Anderson, K., Astort, A., Bodart, O., Cannavò, F., Currenti, G., Dabaghi, F., Erickson, B.A., Garg, D., Head, M., Iozzia, A., Kim, Y.C., Le Mével, H., Lizama, C.N., Rucker, C., Silverii, F., Trasatti, E., Zhan, Y., 2023. Understanding the drivers of volcano deformation through geodetic model verification and validation. Bull. Volcanol. 85, 74. https://doi.org/10.1007/s00445-023-01687-4.
Cubellis, E., Ferri, M., Luongo, G., 1995. Internal structures of Campi Flegrei caldera by gravimetric data. J. Volcanol. Geotherm. Res. 65, 147–156. https://doi.org/10.1016/0377-0273(94)00047-K.
D'Auria, L., Giudicepietro, F., Aquino, I., Borriello, G., Del Gaudio, C., Lo Bascio, D., Martini, M., Ricciardi, G.P., Ricciolino, P., Ricco, C., 2011. Repeated fluid-transfer episodes as a mechanism for the recent dynamics of Campi Flegrei caldera (1989–2010). J. Geophys. Res. Solid Earth 116, B04313. https://doi.org/10.1029/2010JB007837.
D'Auria, L., Pepe, S., Castaldo, R., Giudicepietro, F., Macedonio, G., Ricciolino, P., Tizzani, P., Casu, F., Lanari, R., Manzo, M., Martini, M., Sansosti, E., Zinno, I., 2015. Magma injection beneath the urban area of Naples: a new mechanism for the 2012–2013 volcanic unrest at Campi Flegrei caldera. Sci. Rep. 5, 13100. https://doi.org/10.1038/srep13100.
De Martino, P., Dolce, M., Brandi, G., Scarpato, G., Tammaro, U., 2021. The ground deformation history of the neapolitan volcanic area (Campi Flegrei caldera, Somma–Vesuvius Volcano, and Ischia island) from 20 years of continuous GPS observations (2000–2019). Remote Sens. (Basel) 13, 2725. https://doi.org/10.3390/rs13142725.
De Matteo, A., Massa, B., Castaldo, R., D'Auria, L., James, M.R., Lane, S.J., Pepe, S., Tizzani, P., 2022. An integrated modeling approach for analyzing the deformation style of active volcanoes: Somma-Vesuvius case study. J. Geophys. Res. Solid Earth 127. https://doi.org/10.1029/2021JB022338 e2021JB022338.
De Natale, G., Troise, C., Pingue, F., Mastrolorenzo, G., Pappalardo, L., Battaglia, M., Boschi, E., 2006. The Campi Flegrei caldera: unrest mechanisms and hazards. Geol. Soc. Lond. Spec. Publ. 269, 25–45. https://doi.org/10.1144/gsl.sp.2006.269.01.03.
De Siena, L., Chiodini, G., Vilardo, G., Del Pezzo, E., Castellano, M., Colombelli, S., Tisato, N., Ventura, G., 2017. Source and dynamics of a volcanic caldera unrest: Campi Flegrei, 1983–84. Sci. Rep. 7, 8099. https://doi.org/10.1038/s41598-017-08192-7.
Del Gaudio, C., Aquino, I., Ricciardi, G.P., Ricco, C., Scandone, R., 2010. Unrest episodes at Campi Flegrei: a reconstruction of vertical ground movements during 1905–2009. J. Volcanol. Geotherm. Res. 195, 48–56. https://doi.org/10.1016/j.jvolgeores.2010.05.014.
Deng, F., Rodgers, M., Xie, S., Dixon, T.H., Charbonnier, S., Gallant, E.A., López Vélez, C. M., Ordoñez, M., Malservisi, R., Voss, N.K., Richardson, J.A., 2019. High-resolution DEM generation from spaceborne and terrestrial remote sensing data for improved volcano hazard assessment - a case study at Nevado del Ruiz, Colombia. Remote Sens. Environ. 233, 111348. https://doi.org/10.1016/j.rse.2019.111348.
Di Traglia, F., De Luca, C., Manzo, M., Nolesini, T., Casagli, N., Lanari, R., Casu, F., 2021. Joint exploitation of space-borne and ground-based multitemporal InSAR measurements for volcano monitoring: the Stromboli volcano case study. Remote Sens. Environ. 260, 112441. https://doi.org/10.1016/j.rse.2021.112441.
Di Vito, M., Acocella, V., Aiello, G., Barra, D., Battaglia, M., Caracdente, A., Del Gaudio, C., de Vita, S., Riccciardi, G.P., Scandone, R., Terrasi, F., 2016. Magma transfer at Campi Flegrei caldera (Italy) before the 1538 AD eruption. Sci. Rep. 6, 32245. https://doi.org/10.1038/srep32245.
Dvorak, J.J., Berrino, G., 1991. Recent ground movement and seismic activity in Campi Flegrei, southern Italy: episodic growth of a resurgent dome. J. Geophys. Res. Solid Earth 96, 2309–2323. https://doi.org/10.1029/90JB02225.
Dvorak, J.J., Dzurisin, D., 1997. Volcano geodesy; the search for magma reservoirs and the formation of eruptive event. Rev. Geophys. 35, 343–384. https://doi.org/10.1029/97RG00070.
Dzurisin, D., 2007. Volcano Deformation: Geodetic Monitoring Techniques. Springer-Praxis Books in Geophysical Sciences. Praxis Publishing Ltd., Chichester, UK. ISBN 978-3-540-49302-0.
Falanga, M., Aquino, I., De Lauro, E., Petrosino, S., Ricco, C., 2023. New insights on ground deformation at Campi Flegrei caldera inferred from kinematics and dynamics investigation of borehole tilt. Earth Space Sci. 10. https://doi.org/10.1029/2022EA002702 e2022EA002702.
Fernández, J., Tiampo, K.F., Rundle, J.B., 2001. Viscoelastic displacement and gravity changes due to point magmatic intrusions in a gravitational layered solid Earth. Geophys. J. Int. 146, 155–170. https://doi.org/10.1046/j.0956-540x.2001.01450.x.
Fernández, J., Tizzani, P., Manzo, M., Borgia, A., González, P.J., Martí, J., Pepe, A., Camacho, A.G., Casu, F., Berardino, P., Prieto, J.F., Lanari, R., 2009. Gravity-driven deformation of Tenerife measured by InSAR time series analysis. Geophys. Res. Lett. 36. https://doi.org/10.1029/2008GL036920. L04306.
Fernández, J., Pepe, A., Poland, M.P., Sigmundsson, F., 2017. Volcano geodesy: recent developments and future challenges. J. Volcanol. Geotherm. Res. 344, 1–12. https://doi.org/10.1016/j.jvolgeores.2017.08.006.
Fernández, J., Escayo, J., Hu, Z., Camacho, A.G., Samsonov, S.V., Prieto, J.F., Tiampo, K. F., Palano, M., Mallorquí, J.J., Ancochea, E., 2021. Detection of volcanic unrest onset in La Palma, Canary Islands, evolution and implications. Sci. Rep. 11, 2540. https://doi.org/10.1038/s41598-021-82292-3.
Fernández, J., Escayo, J., Camacho, A.G., Palano, M., Prieto, J.F., Hu, Z., Samsonov, S.V., Tiampo, K.F., Ancochea, E., 2022. Shallow magmatic intrusion evolution below La Palma before and during the 2021 eruption. Sci. Rep. 12, 20257. https://doi.org/10.1038/s41598-022-23998-w.
Fernández, J., Escayo, J., Prieto, J.F., Tiampo, K.F., Camacho, A.G., Ancochea, E., 2024. Volcanic unrest after the 2021 eruption of La Palma. Geophys. Res. Lett. 51. https://doi.org/10.1029/2024GL108803 e2024GL108803.
Florio, G., Fedi, M., Cella, F., Rapolla, A., 1999. The Campanian Plain and Phlegrean Fields: structural setting from potential field data. J. Volcanol. Geotherm. Res. 91, 361–379. https://doi.org/10.1016/S0377-0273(99)00044-X.
Gabriel, A.K., Goldstein, R.M., Zebker, H.A., 1989. Mapping small elevation changes over large areas: differential interferometry. J. Geophys. Res. Solid Earth 94, 9183–9191. https://doi.org/10.1029/JB094iB07p09183.
Gallo, R.I., Ort, M.H., Iacovino, K., Silleni, A., Smith, V.C., Giordano, G., Isaia, R., Boro, J., 2024. Reconciling complex stratigraphic frameworks reveals temporally and geographically variable depositional patterns of the Campanian Ignimbrite. Geosphere 20, 1–22. https://doi.org/10.1130/GES02651.1.
Geertsma, J., Van Opstal, G., 1973. A numerical technique for predicting subsidence above compacting reservoirs based on the nucleus of strain concept. Verh. Kon. Ned. Geol. Mijnbouwk 28, 63–78.
Gola, G., Barone, A., Castaldo, R., Chiodini, G., D'Auria, L., García-Hernández, R., Pepe, S., Solaro, G., Tizzani, P., 2021. A novel multidisciplinary approach for the thermo-rheological study of volcanic areas: the case study of Long Valley caldera. J. Geophys. Res. Solid Earth 126. https://doi.org/10.1029/2020JB020331 e2020JB020331.
González, P.J., Samsonov, S.V., Pepe, S., Tiampo, K.F., Tizzani, P., Casu, F., Fernández, J., Camacho, A.G., Sansosti, E., 2013. Magma storage and migration associated with the 2011-2012 El Hierro eruption: implications for crustal magmatic systems at oceanic island volcanoes. J. Geophys. Res. Solid Earth 118, 4361–4377. https://doi.org/10.1002/jgrb.50289.
Isaia, R., Marianelli, P., Sbrana, A., 2009. Caldera unrest prior to intense volcanism in Campi Flegrei (Italy) at 4.0 ka B.P.: implications for caldera dynamics and future eruptive scenarios. Geophys. Res. Lett. 36, L21303. https://doi.org/10.1029/2009GL040513.
Isaia, R., Di Giuseppe, M.G., Natale, J., Tramparulo, F.D.A., Troiano, A., Vitale, S., 2021. Volcano-tectonic setting of the Pisciarelli fumarole field, Campi Flegrei caldera, southern Italy: insights into fluid circulation patterns and hazard scenarios. Tectonics 40. https://doi.org/10.1029/2020TC006227 e2020TC006227.
Jo, M.-J., Jung, H.-S., Won, J.-S., Lundgren, P., 2015. Measurement of three-dimensional surface deformation by Cosmo-SkyMed X-band radar interferometry: application to the March 2011 Kamoamoa fissure eruption, Kilauea Volcano, Hawai'i. Remote Sens. Environ. 169, 176–191. https://doi.org/10.1016/j.rse.2015.08.00.
Jolivet, R., Grandin, R., Lasserre, C., Doin, M.-P., Peltzer, G., 2011. Systematic InSAR tropospheric phase delay corrections from global meteorological reanalysis data. Geophys. Res. Lett. 38, L17311. https://doi.org/10.1029/2011GL048757.
Kennedy, B., Wilcock, J., Stix, J., 2012. Caldera resurgence during magma replenishment and rejuvenation at Valles and Lake City calderas. Bull. Volcanol. 74, 1833–1847. https://doi.org/10.1007/s00445-012-0641-x.
Kubanek, J., Westerhaus, M., Schenk, A., Aisyah, N., Brotopuspito, K.S., Heck, B., 2015. Volumetric change quantification of the 2010 Merapi eruption using TanDEM-X InSAR. Remote Sens. Environ. 164, 16–25. https://doi.org/10.1016/j.rse.2015.02.027.
Lanari, R., Berardino, P., Borgström, S., Del Gaudio, C., De Martino, P., Fornaro, G., Guarino, S., Sansosti, E., Lundgren, P., 2004. The use of IFSAR and classical geodetic techniques for caldera unrest episodes: application to the Campi Flegrei uplift event of 2000. J. Volcanol. Geotherm. Res. 133, 247–260. https://doi.org/10.1016/S0377-0273(03)00401-3.
Lisowski, M., 2007. Analytical volcano deformation source models. In: Dzurisin, D. (Ed.), Volcano Deformation. Springer Praxis Books Springer, Berlin, Heidelberg, pp. 270–304. https://doi.org/10.1007/978-3-540-49302.
Loughlin, S.C., Sparks, S., Brown, S.K., Jenkins, S.F., Vye-Brown, C., 2015. Global Volcanic Hazards and Risk. Cambridge University Press.
Luongo, G., Cubellis, E., Obrizzo, F., Petrazzuoli, S.M., 1991. A physical model for the origin of volcanism of the Tyrrhenian margin: the case of Neapolitan area. J. Volcanol. Geotherm. Res. 48, 173–185. https://doi.org/10.1016/0377-0273(91)90041-W.
Massonnet, D., Rossi, M., Carmona, C., Adragna, F., Peltzer, G., Feigl, K., Rabaute, T., 1993. The displacement field of the landers earthquake mapped by radar interferometry. Nature 364, 138–142. https://doi.org/10.1038/364138a0.
Naranjo, C., Euillades, P., Toyos, G., Euillades, L., Villarosa, G., 2023. Application of a temporal decorrelation model using Sentinel-1 SAR data to detect volcanic ash deposits related to the 2020 Taal volcano eruption. Remote Sens. Appl. Soc. Environ. 31, 100991. https://doi.org/10.1016/j.rsase.2023.100991.
Natale, J., Camanni, G., Ferranti, L., Isaia, R., Sacchi, M., Spiess, V., Steinmann, L., Vitale, S., 2022. Fault systems in the offshore sector of the Campi Flegrei caldera (southern Italy): implications for nested caldera structure, resurgent dome, and volcano-tectonic evolution. J. Struct. Geol. 163, 104723. https://doi.org/10.1016/j.jsg.2022.104723.
Natale, J., Vitale, S., Repola, L., Monti, L., Isaia, R., 2024. Geomorphic analysis of digital elevation model generated from vintage aerial photographs: a glance at the pre-urbanization morphology of the active Campi Flegrei caldera. Geomorphology 460, 109267. https://doi.org/10.1016/j.geomorph.2024.109267.
Nespoli, M., Tramelli, A., Belardinelli, M.E., Bonafede, M., 2023. The effects of hot and pressurized fluid flow across a brittle layer on the recent seismicity and deformation

in the Campi Flegrei caldera (Italy). J. Volcanol. Geotherm. Res. 443, 107930. https://doi.org/10.1016/j.jvolgeores.2023.107930.
Okada, Y., 1985. Surface deformation due to shear and tensile faults in a half-space. BSSA 75, 1135–1154. https://doi.org/10.1785/BSSA0750041135.
Orsi, G., D'Antonio, M., de Vita, S., Gallo, G., 1992. The Neapolitan yellow tuff, a large-magnitude trachytic phreatoplinian eruption: eruptive dynamics, magma withdrawal and caldera collapse. J. Volcanol. Geotherm. Res. 53, 275–287. https://doi.org/10.1016/0377-0273(92)90086-S.
Orsi, G., Di Vito, M.A., Isaia, R., 1999. Volcanic hazard assessment at the Campi Flegrei caldera. J. Volcanol. Geotherm. Res. 91, 243–263. https://doi.org/10.1016/S0377-0273(99)00037-1.
Pepe, A., Lanari, R., 2006. On the extension of the minimum cost flow algorithm for phase unwrapping of multitemporal differential SAR interferograms. IEEE Trans. Geosci. Remote Sens. 44, 2374–2383. https://doi.org/10.1109/TGRS.2006.873207.
Pepe, S., De Siena, L., Barone, A., Castaldo, R., D'Auria, L., Manzo, M., Casu, F., Fedi, M., Lanari, R., Bianco, F., Tizzani, P., 2019. Volcanic structures investigation through SAR and seismic interferometric methods: the 2011–2013 Campi Flegrei unrest episode. Remote Sens. Environ. 234, 111440. https://doi.org/10.1016/j.rse.2019.111440.
Petrillo, Z., Tripaldi, S., Mangiacapra, A., Scippacercola, S., Caliro, S., Chiodini, G., 2023. Principal component analysis on twenty years (2000−2020) of geochemical and geophysical observations at Campi Flegrei active caldera. Sci. Rep. 13, 18445. https://doi.org/10.1038/s41598-023-45108-0.
Poland, M.P., Zebker, H.A., 2022. Volcano geodesy using InSAR in 2020: the past and next decades. Bull. Volcanol. 84, 27. https://doi.org/10.1007/s00445-022-01531-1.
Polcari, M., Borgstrom, S., Del Gaudio, C., De Martino, P., Ricco, C., Siniscalchi, V., Trasatti, E., 2022. Thirty years of volcano geodesy from space at Campi Flegrei caldera (Italy). Sci. Data 9, 728. https://doi.org/10.1038/s41597-022-01849-7.
Pritchard, M.E., Mather, T.A., McNutt, S.R., Delgado, F.J., Reath, K., 2019. Thoughts on the criteria to determine the origin of volcanic unrest as magmatic or non-magmatic. Phil. Trans. R. Soc. A 377, 20180008. https://doi.org/10.1098/rsta.2018.0008.
Rosen, P.A., Hensley, S., Joughin, I.R., Li, F.K., Madsen, S.N., Rodriguez, E., Goldstein, R., 2000. Synthetic aperture radar interferometry. IEEE Proc. 88, 333–376. https://doi.org/10.1109/5.838084.
Rosi, M., Sbrana, A., 1987. Phlegraean Fields, Quaderni de" La Ricerca Scientifica", 114 CNR. Roma 114–175.
Samsonov, S.V., Tiampo, K.F., Camacho, A.G., Fernández, J., González, P.J., 2014. Spatiotemporal analysis and interpretation of 1993–2013 ground deformation at Campi Flegrei, Italy, observed by advanced DInSAR. Geophys. Res. Lett. 41, 6101–6108. https://doi.org/10.1002/2014GL060595.
Saroli, M., Albano, M., Atzori, S., Moro, M., Tolomei, C., Bignami, C., Stramondo, S., 2021. Analysis of a large seismically induced mass movement after the December 2018 Etna volcano (southern Italy) seismic swarm. Remote Sens. Environ. 263, 112524. https://doi.org/10.1016/j.rse.2021.112524.
Scotto di Uccio, F., Lomax, A., Natale, J., Muzellec, T., Festa, G., Nazeri, S., Convertito, V., Bobbio, A., Strumia, C., Zollo, A., 2024. Delineation and fine-scale structure of fault zones activated during the 2014–2024 unrest at the Campi Flegrei caldera (Southern Italy) from high-precision earthquake locations. Geophys. Res. Lett. 51. https://doi.org/10.1029/2023GL107680 e2023GL107680.
Sibson, R.H., 1974. Frictional constraints on thrust, wrench and normal faults. Nature 249, 542–544. https://doi.org/10.1038/249542a0.
Sigmundsson, F., Hreinsdóttir, S., Hooper, A., Árnadóttir, T., Pedersen, R., Roberts, M.J., Óskarsson, N., Auriac, A., Decriem, J., Einarsson, P., Geirsson, H., Hensch, M., Ófeigsson, B.G., Sturkell, E., Sveinbjörnsson, H., Feigl, K.L., 2010. Intrusion triggering of the 2010 Eyjafjallajökull explosive eruption. Nature 468, 426–430. https://doi.org/10.1038/nature09558.
Siniscalchi, A., Tripaldi, S., Romano, G., Chiodini, G., Improta, L., Petrillo, Z., D'Auria, L., Caliro, S., Avino, R., 2019. Reservoir structure and hydraulic properties of the Campi Flegrei geothermal system inferred by audiomagnetotelluric, geochemical, and seismicity study. J. Geophys. Res. Solid Earth. 124, 5336–5356. https://doi.org/10.1029/2018JB016514.
Sparks, R.S.J., Biggs, J., Neuberg, J.W., 2012. Monitoring volcanoes. Science 335, 1310–1311. https://doi.org/10.1126/science.1219485.
Tizzani, P., Battaglia, M., Castaldo, R., Pepe, A., Zeni, G., Lanari, R., 2015. Magma and fluid migration at Yellowstone caldera in the last three decades inferred from InSAR, leveling, and gravity measurements. J. Geophys. Res. Solid Earth 120, 2627–2647. https://doi.org/10.1002/2014JB011502.
Tramelli, A., Giudicepietro, F., Ricciolino, P., Chiodini, G., 2022. The seismicity of Campi Flegrei in the contest of an evolving long term unrest. Sci. Rep. 12, 2900. https://doi.org/10.1038/s41598-022-06928-8.
Trasatti, E., Giunchi, C., Agostinetti, N.P., 2008. Numerical inversion of deformation caused by pressure sources: application to Mount Etna (Italy). Geophys. J. Int. 172, 873–884. https://doi.org/10.1111/j.1365-246X.2007.03677.x.
Troiano, A., Di Giuseppe, M.G., Isaia, R., 2022. 3D structure of the Campi Flegrei caldera central sector reconstructed through short-period magnetotelluric imaging. Sci. Rep. 12, 20802. https://doi.org/10.1038/s41598-022-24998-6.
Troise, C., De Natale, G., Schiavone, R., Somma, R., Moretti, R., 2019. The Campi Flegrei caldera unrest: discriminating magma intrusions from hydrothermal effects and implications for possible evolution. Earth Sci. Rev. 188, 108–122. https://doi.org/10.1016/j.earscirev.2018.11.007.
Vitale, S., Isaia, R., 2014. Fractures and faults in volcanic rocks (Campi Flegrei, southern Italy): insight into volcano-tectonic processes. Int. J. Earth Sci. (Geol. Rundsch.) 103, 801–819. https://doi.org/10.1007/s00531-013-0979-0.
Vitale, S., Natale, J., 2023. Combined volcano-tectonic processes for the drowning of the Roman western coastal settlements at Campi Flegrei (southern Italy). EPS 75, 38. https://doi.org/10.1186/s40623-023-01795-7.
Widiwijayanti, C., Thin Zar Win, N., Espinosa-Ortega, T., Costa, F., Taisne, B., 2024. The global volcano monitoring infrastructure database (GVMID). Front. Earth Sci. 12, 1284889. https://doi.org/10.3389/feart.2024.1284889.
Wohletz, K., Civetta, L., Orsi, G., 1999. Thermal evolution of the Phlegraean magmatic system. J. Volcanol. Geotherm. Res. 91, 381–414. https://doi.org/10.1016/S0377-0273(99)00048-7.
Woo, J.Y.L., Kilburn, C.R.J., 2010. Intrusion and deformation at Campi Flegrei, southern Italy: sills, dikes, and regional extension. J. Geophys. Res. Solid Earth 115, B12210. https://doi.org/10.1029/2009JB006913.
Zollo, A., Maercklin, N., Vassallo, M., Dello Iacono, D., Virieux, J., Gasparini, P., 2008. Seismic reflections reveal a massive melt layer under Campi Flegrei volcanic field. Geophys. Res. Lett. 35, L12306. https://doi.org/10.1029/2008GL034242.